DETERMINING THE sp^2/sp^3 BONDING CONCENTRATIONS OF CARBON FILMS

A Thesis Submitted to the College of

Graduate Studies and Research

in Partial Fulfillment of the Requirements

for the Degree of Master of Science

in the Department of Physics and Engineering Physics

University of Saskatchewan

Saskatoon

By

TRENTON DAVID HAMILTON

Keywords: amorphous carbon, PTFE, nanodiamond, graphite, C_{60}, synchrotron radiation, soft x-ray spectroscopy.

PERMISSION TO USE

In presenting this thesis in partial fulfillment of the requirements for a Postgraduate degree from the University of Saskatchewan, I agree that the Libraries of this University may make it freely available for inspection. I further agree that permission for copying of this thesis in any manner, in whole or in part, for scholarly purposes may be granted by Alexander Moewes or, in his absence, by the Head of the Department of Physics and Engineering Physics. It is understood that any copying or publication or use of this thesis or parts thereof for financial gain shall not be allowed without my written permission. It is also understood that due recognition shall be given to me and to the University of Saskatchewan in any scholarly use which may be made of any material in my thesis.

Requests for permission to copy or to make other use of material in this thesis in whole or part should be addressed to:

Alexander Moewes
116 Science Place
Saskatoon, Saskatchewan S7N 5E2
Canada

ABSTRACT

Analysis of the electronic structures of nitrogen-doped, amorphous carbon samples and of nanodiamond films are carried out in order to determine their sp^2 bonding concentration. The amorphous carbon samples under consideration are deposited onto polytetrafluoroethylene (PTFE) polymer substrates by hot wire plasma sputtering of graphite in varying nitrogen concentration atmospheres. The deposition or modification of the substrate's surface may lend itself to increasing hardness and wear resistance. Eventually these polymer substrates may be used for applications in the field of biomaterials, focusing on cardiovascular surgery, where a low blood/surface interaction is important.

The primary technique used in this study is x-ray absorption spectroscopy, measured at the Advanced Light Source synchrotron at the Lawrence Berkeley National Laboratory, Berkeley, USA. A method of analyzing these spectra was then developed to determine the sp^2 bonding concentrations in carbon films.

Through this newly developed analysis method, the sp^2 bonding concentrations in these samples increases from 74 to 93% with growing nitrogen doping. The diamond films presented here are deposited on silicon wafer substrates in a methane atmosphere by microwave plasma deposition. Various deposition conditions, such as bias voltage and methane atmosphere concentration, affect the purity of the diamond film. This analysis reveals sp^2 bonding concentrations in these samples from, typically, a few percent to 25%.

ACKNOWLEDGEMENTS

My supervisor, Alexander Moewes, provided me with an excellent opportunity to grow as a student and person, and lead by example. Without his leadership none of this would have been possible. Qiaoqin Yang and Mikhail Foursa prepared the nanodiamond and a-C samples studied in this project. My colleagues have always been available to teach me physics and made this a great working environment. Work at the Advanced Light Source at Lawrence Berkeley National Laboratory is supported by the US Department of Energy (Contract DE-AC03-76SF00098). Alexander Moewes is a Canada Research Chair. Most importantly my wife, Brianne, has somehow found it in herself to put up with me and care for me during all this time; her love and understanding is unparalleled.

TABLE OF CONTENTS

LIST OF FIGURES

LIST OF ABBREVIATIONS AND PARAMETERS

ALS	Advanced Light Source at Lawrence Berkeley National Laboratory
a-C	Amorphous Carbon
CB	Conduction Band
DOS	Density of States
E_B	Binding Energy
EELS	Electron Energy Loss Spectroscopy
E_{kin}	Kinetic Energy
HOPG	Highly Oriented Pyrolytic Graphite
$h\nu_{exc}$	Photon Excitation Energy
IP	Ionization Potential
$I_{ref\pi^*}$	Integral Area of π^* Resonances in Absorption Spectrum of Reference Sample
$I_{ref}(\Delta E)$	Total Integral Area of Absorption Spectrum of Reference Sample
$I_{u\pi^*}$	Integral Area of π^* Resonances in Absorption Spectrum of Unknown Carbon Sample
$I_u(\Delta E)$	Total Integral Area of Absorption Spectrum of Unknown Carbon Sample
PFY	Partial Fluorescence Yield
PTFE	Polytetrafluoroethylene
TEY	Total Electron Yield
TFY	Total Fluorescence Yield
VB	Valence Band
XAS	X-Ray Absorption Spectroscopy
XES	X-Ray Emission Spectroscopy
XPS	X-Ray Photoemission Spectroscopy

Φ_{work}	Work Function
ω_k	K-Shell Fluorescence Yield
γ	Lorentz Factor

INTRODUCTION

From a technological point of view, amorphous carbon (a-C) is an attractive material. It can be nearly as hard as diamond; it is chemically inert and has a very small roughness [1]. Films with high content of sp^3 hybridized carbon atoms have been associated with mechanical applications because of these properties [2]. These properties make them attractive for a variety of other applications, such as increased wear lifetime, protective layers for magnetic recording disks, and as cathodes in flat panel field emission displays [3 – 6]. Plasma-assisted deposition of a-C films on polymer substrates is a technique for modifying the substrate surface, where layers of these a-C films may be a promising base coating to manage biological reactions or improve surface conductivity of the substrate [7]. Fluorocarbon polymers are used for applications in the field of biomaterials for cardiovascular surgery [8], where carbon deposition or modification of the polymer's surface may increase hardness and wear resistance, and lower blood/surface interaction.

The subject of this work is to develop a new model for determining the sp^2 bonding concentration in carbon samples, which will serve to link their electronic structure with their physical properties. Plasma-assisted deposition of carbon films for the purposes of field emission displays, protective coating layers on magnetic recording devices, mechanical applications and cardiovascular surgery will be greatly aided by a consistent and reliable method of determining the sp^2 concentration of the film. Prior to deposition, deposition parameters will be customized to yield a desired sp^2 bonding concentration of a film. Deficiencies in earlier models are addressed and this new model is applied to a-C and nanodiamond films, with the opportunity to evaluate other carbon allotropes, such as nanotubes, nanofibres and nanocones.

In the first section of this thesis we present the experimental setup of beamline 8.0.1 of the ALS and the measurement techniques used for this study. The second section includes discussion on theory, including hybridization and bonding in carbon allotropes, specifically fullerenes, graphite, diamond and amorphous carbons. The third section details the newly developed analysis technique, presents spectroscopic data on amorphous carbon and diamond films, and the results of analysis.

1 EXPERIMENTAL

1.1 Synchrotron Radiation

High brilliance x-rays are produced at synchrotron light sources, which operate on the principle that accelerated charges emit photons. In practice, electrons are accelerated to relativistic speeds then confined by bending magnets to travel within a storage ring. While traveling in a circular path in the storage ring they emit a narrow cone of tangential radiation. This radiation is neither highly focused nor monochromatic.

Insertion devices are placed in straight sections of the storage ring, which increase the brilliance of radiation, defined as the photon flux impinging on the sample per unit area per unit solid angle in a 0.1% energy bandwidth (units of photons/sec/mm^2/mrad^2 in a 0.1% energy bandwidth), beyond bending magnet radiation. An undulator insertion device (Fig. 1.1) is an array of magnets designed to generate quasi-monochromatic electromagnetic radiation. Because of the alternating magnetic field of the magnets, electrons traveling through the undulator experience periodic transverse forces. The electron beam radiates in the forward direction at each peak of the sinusoidal trajectory. To the electron, the radiation wavelength is the undulator period divided by γ due to relativistic Lorentz contraction. In the laboratory frame of reference this wavelength appears to the observer (workstation) further reduced by another factor of γ due to the Doppler effect. The undulator period length, defined as the distance between like magnetic poles of the undulator, 5.0 cm in the case of beamline 8.0.1 of the ALS, is thus

reduced by a factor of γ^2 to yield radiation in the soft x-ray regime. Due to the relatively weak magnetic fields in the undulator, the amplitude of oscillation is small. Thus, the radiation cone is narrow, and the brilliance is typically a few orders of magnitude higher than in wigglers and bending magnets. Tuning the undulator gap width to different harmonics enables for maximum flux at the expense of resolving power (E/ΔE), where E is the energy of the exciting radiation and ΔE is the energy resolution.

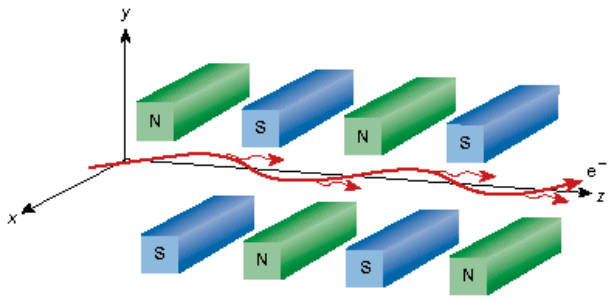

Fig. 1.1. Path of an electron through an undulator [9].

1.1.1 Beamline 8.0.1 Setup

Radiation from the undulator (Fig. 1.2) is focused onto the water-cooled, movable entrance slit by a vertical condensing mirror. Light then reaches one of the inter-changeable spherical gratings of the monochromator at a grazing incidence angle, which is then passed through an exit slit towards the sample. The optimal focusing condition is met when the entrance slit, grating, and exit slit satisfy Rowland Geometry [10]. A more detailed description of the setup at beamline 8.0.1 can be found in [10, 11]. At the maximum resolving power (E/ΔE) of 10^4 for absorption spectra (Fig. 1.3), the flux on the sample may reach 10^{12} photons/second. Flux can be increased a few orders of magnitude, at the expense of resolving power, for shorter spectral acquisition time. High resolution absorption spectra with high signal to noise ratios require more time to acquire than lower resolution spectra of the same signal to noise ratio.

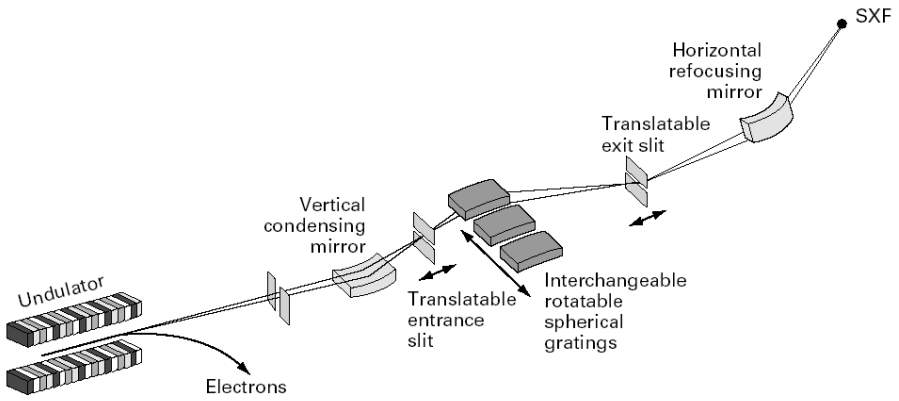

Fig. 1.2. Beamline 8.0.1 setup at the ALS [12].

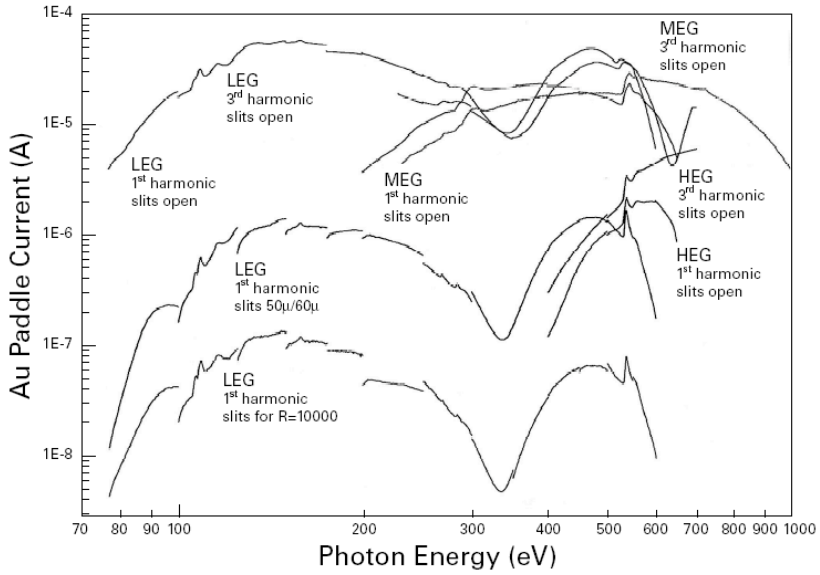

Fig. 1.3. The monochromator operates in both the first and second orders with three gratings (LEG, MEG, HEG) with line densities of 150, 380, 925 lines/mm. The flux was measured for an entrance-slit width of 50 µm, an exit-slit width of 60 µm, and an optimized exit-slit position. The curves give the results of measurements made at various harmonics of the U5 undulator with the ALS operating at 1.9 GeV, normalized to a 400 mA beam current. The flux with slits narrowed to give a calculated resolving power of 10,000 is about 10^{12} photons/sec. [12].

1.2 X-Ray Absorption Spectroscopy

X-ray absorption spectroscopy (XAS) is a technique used to probe the local partial unoccupied electronic density of states in an atom and thusly their chemical bonding state. XAS is most sensitive to the short-range order of atoms, or an atom's nearest neighbors. An absorbed photon of sufficient energy will promote a core level electron to a higher energy unoccupied state (Fig. 1.4) according to dipole transition rules ($\Delta l = \pm 1$, $\Delta m = \pm 1$ or 0).

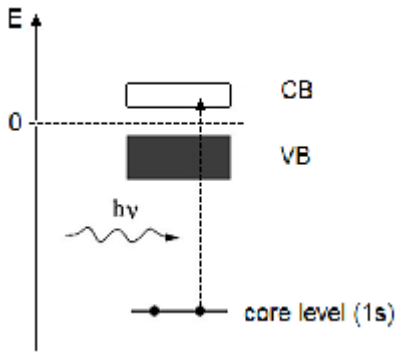

Fig. 1.4. Excitation of an electron from the core level to unoccupied CB states.

In XAS, instrumental, core hole lifetime, and final state lifetime broadening widen spectral features. Instrumental broadening is due to the optics and environment of the measurements, generally quantified by the resolving power ($E/\Delta E$). Instrumental broadening is modeled by a Gaussian function with a standard deviation, or full width at half maximum (FWHM), derived from the resolving power. The short lifetime of a core hole causes a broadening (Γ, FWHM) in the energy of the state based on the Heisenberg uncertainty principle

$$\Gamma = \frac{\hbar}{\tau_h}, \qquad (1.1)$$

where τ_h is the core hole lifetime. Similarly, final state lifetime (τ_f) broadening is due to the limited lifetime of the system after absorption or emission. There is an

electron (core hole) left in the conduction (valence) band after absorption (emission), which has a limited lifetime before decay. The lifetime causes an uncertainty in that state's energy value, broadening its spectrum. Both core hole and final state broadenings are modeled with Lorentzian functions [13].

At BL 8.0.1 of the ALS three methods are used to conduct XAS experiments: total electron yield (TEY), total fluorescence yield (TFY), and partial fluorescence yield (PFY), which are described in the following.

1.2.1 Total Electron Yield

In total electron yield mode the number of electrons escaping the sample is counted. Photoionization and Auger decay, depicted in Fig. 1.5, are two processes that leave a net positive charge on the sample. Photoionization is photon absorption by the atom with the emission of a photoelectron of kinetic energy equal to the photon energy minus the binding energy and work function of the material. A core hole is predominantly refilled through Auger decay [14]. In this process, the electronic transition energy is transferred to another electron, which is emitted. The current needed to neutralize the sample as a function of energy represents the absorption spectrum and is a direct measure of the partial density of states. An absorption spectrum depends, to some extent, on the conductivity of the sample. If it is highly conductive then current can easily flow into the sample to quickly refill the core holes and thus correctly represents the absorption spectrum. If it is insulating then current will not easily flow through the sample, thus underestimating the actual absorption. The detection depth of TEY measurements, governed by the escape depth of electrons, in this energy range is about 12 Å [15, 16], as shown in Fig. 1.6.

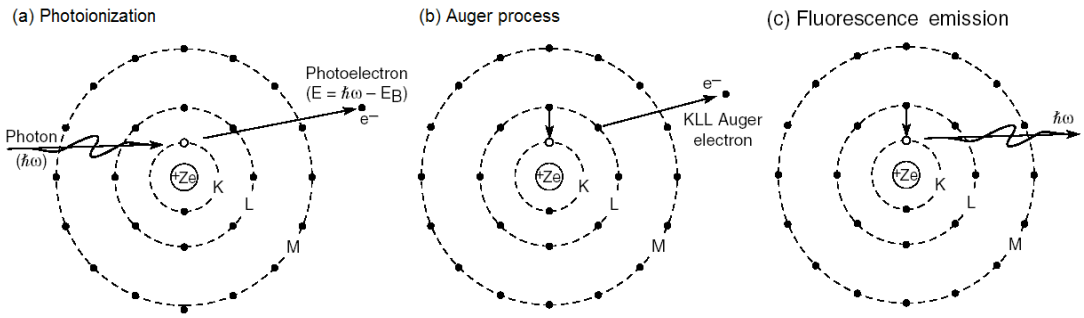

Fig. 1.5. (a) An incident photon of sufficient energy ħω is absorbed by the atom with the emission of a photoelectron of kinetic energy equal to the photon energy minus the binding energy minus the sample's work function. A vacancy is created, eventually to be filled by an outer electron. (b) The atom adjusts to the core vacancy through the non-radiative Auger process in which one electron makes a transition to the core vacancy, while a second electron of characteristic energy is emitted. (c) An atom with a core hole vacancy readjusts as a higher-lying electron makes a transition to the vacancy, with the emission of a photon of characteristic energy [17].

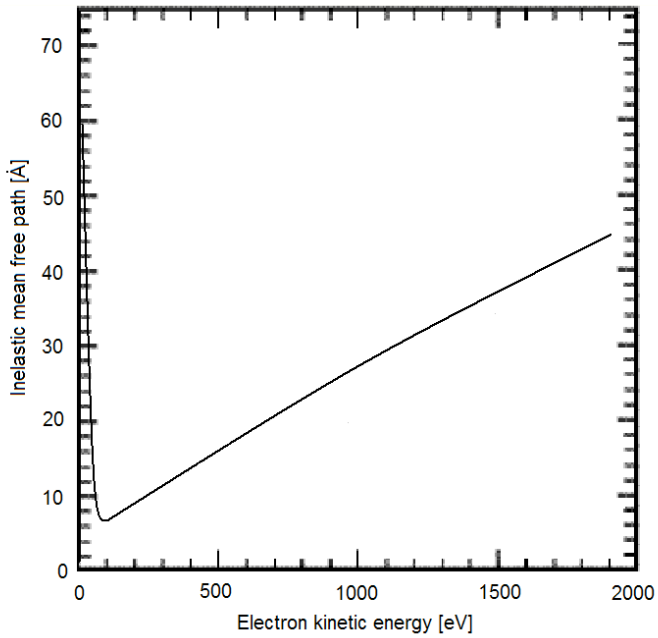

Fig. 1.6. Inelastic mean free path for energies up to 2000 eV in carbon [18].

1.2.2 Total Fluorescence Yield

An electron can make a dipole transition from a higher lying level to a core hole emitting a photon with energy equal to the energy difference in those levels. The number of fluorescence photons is directly related to the number of absorbed photons. Total fluorescence yield (TFY) measures all the fluorescence photons, within its sensitivity range, emitted from the sample impinging on the channeltron detector. A channeltron is a cascade multiplier that produces a signal proportional to the number of photons striking it. The number of fluorescence photons detected from the sample as a function of excitation energy represents TFY absorption.

1.2.3 Partial Fluorescence Yield

Finally, partial fluorescence yield (PFY) measures the fluorescence photons within a certain energy range and therefore associated with a particular electronic transition. The fluorescence spectrometer detects all photons within that energy range as a function of excitation energy. Again, since the number of fluorescence photons is directly related to the number of absorbed photons, PFY similarly represents the absorption.

Fluorescence yield measurements are relatively bulk-sensitive, since the attenuation length of photons in carbon in this energy range is about 100 nm [11, 19], approximately 80 times that of electrons. Incident radiation will excite carbon atoms anywhere from the sample's surface to approximately a 100 nm depth. A fluorescence photon created from up to a 100 nm depth has an equal chance of escaping the sample as the likelihood of incident radiation reaching that depth. In electron yield measurements, emitted electrons have a much lower escape depth than photons.

1.3 X-Ray Emission Spectroscopy

X-ray emission spectroscopy (XES) is a technique used to probe the occupied electronic states in a material. X-ray emission is produced when a core electron is excited by an absorbed photon and this excited state decays by emitting a photon when the core hole is filled, as shown in Fig. 1.7. The energy of the emitted photon equals the energy difference between the core hole level and the state from which the electron came. Generally, valence electrons fall to the core level providing a picture of the occupancy of valence states [20]. The XES spectrum displays intensity, or count rate, versus emission energy.

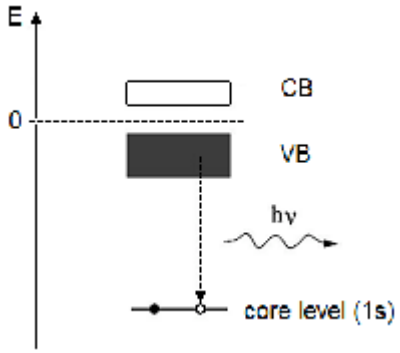

Fig. 1.7. Decay of a core hole with the VB emission of a photon.

Fluorescence is not the dominant relaxation process for low atomic number atoms [17]. Below Z = 30, K-shell Auger dominates over fluorescence, and below Z = 90, L_3-subshell Auger dominates over fluorescence. As many as 10^4 core holes are needed in order to create one fluorescence photon in our energy range in carbon due to the dominance of competing non-radiative Auger transitions [21, 22]. Effective K-shell fluorescence yields for carbon based on theoretical and experimental data are listed in Table 1.1. The fluorescence yield represents the number of fluorescence photons emitted per K-shell vacancy during the relaxation process. Discrepancies in these fluorescence yield values arise from the various methods of estimation and empirical data collection.

Table 1.1. K-shell fluorescence yields for carbon.

ω_k (*10^{-4})	Ref.
8.8	23
35	24
51	25
876	26

1.3.1 Beamline 8.0.1 Spectrometer

The soft x-ray fluorescence endstation at beamline 8.0.1 of the ALS is comprised of a Rowland-circle type grating emission spectrometer with a photon counting area detector and an ultrahigh vacuum sample chamber. The sample chamber is held under ultra-high vacuum by turbomolecular, ion, and sublimation pumps. The sample can be manipulated in the x, y, z, and θ directions. The emission spectrometer has an entrance slit, with a variable width between 0 – 100 μm, allowing for higher resolution emission spectra at narrower slit widths. There are four interchangeable constant groove density spherical Rowland-circle diffraction gratings housed within in a chamber separated from the sample chamber by a valve. The four diffraction gratings have different groove densities in order to diffract different energy ranges. Different emission energy ranges are selected by manually rotating the carousel to the grating with the correct radius and groove density. The energy range covered by these four gratings is 40 – 1000 eV. Mounted behind the grating carousel is an area sensitive Multi-channel plate detector to record the emitted radiation. The detector is 40 mm in diameter with a 512x512 pixel matrix [10]. This combination provides an instrumental resolution of about 0.4 eV at C Kα emission energies. All absorption and emission spectra are normalized to the incident beam current, monitored by a high transmission gold mesh located in front of the sample.

1.4 Spectral Features in XAS

1.4.1 π* and σ* Absorption Features

When discussing electronic structures, it is often useful to speak in terms of atomic or molecular orbitals. Atomic orbitals are states of an electron in an atom, where the orbital can be represented by a wavefunction, similar to an electron density cloud. The square of the wavefunction is proportional to the spatial electron distribution. π, σ, π*, and σ* occupied and unoccupied (*) orbitals are particularly common terms when discussing molecular systems, but are often used for crystal or solid state structures.

In order to explain crystal structure in this fashion, π and σ orbitals in a molecular system must first be discussed. In molecular diatomics, σ orbitals are symmetric with respect to reflection through a plane containing the symmetry axis of the molecule and π orbitals are antisymmetric. In polyatomic molecules, the molecular orbitals involve overlap of the wavefunctions, which is generally more extended, but the resulting orbitals can still be labeled either σ, symmetric, or π, antisymmetric, with respect to the local symmetry plane. Carbon 1s → 2p (CB) transitions are into conduction band states with π and σ symmetry, among others. For K-shell absorption spectra, it is the unfilled orbitals which are of importance, since the observed features correspond to dipole allowed transitions of a core 1s electron to π and σ unoccupied orbitals [27]. Transitions to unoccupied π and σ orbitals are labeled π* and σ*, respectively.

Valence and conduction orbitals significantly overlap with those of neighbouring atoms in crystals generating bands of spatially delocalized energy levels. In diatomic molecules, σ orbitals are in plane and π orbitals are out of plane. Similarly in graphite, for example, σ-like bonding occurs in the plane of the graphite sheets and π-like bonding occurs out of plane. More on the discussion of graphite can be

found in Section 2.3. It is common to refer to bands with π-symmetry and σ-symmetry in crystal structures as π and σ bands, respectively.

Energetically, electrons occupying conduction band states are more loosely bound than those in the valence band. Absorption spectra probe the unoccupied states, so, as shown in Fig. 1.8, π* orbitals, if present, are the energetically lowest features seen [27]. In emission spectra, π orbitals, when present, are the energetically highest structures seen (Fig. 1.8). A π* feature is only seen in absorption spectra of a molecule or crystal with π bonding.

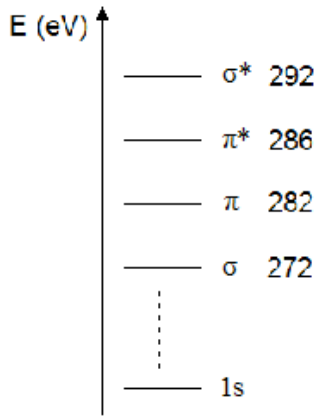

Fig. 1.8. Typical orbital energy levels in a crystal or molecule, with approximate energies for promoting carbon electrons from the 1s shell into the conduction and valence bands.

The link between π, π*, σ, σ* orbitals and sp, sp^2, and sp^3 hybrid orbitals is discussed in detail in Section 2.1.

1.4.2 Excitons

Absorption spectra may show structure below the lowest unoccupied state among others. This structure can be caused by the absorption of a photon with the creation of an electron-hole pair, which is called an exciton. This electron-hole pair is bound by their Coulomb attraction [28 – 31]. An exciton is inherently unstable, since the electron may recombine and refill the hole. Similarly, a core exciton is an electron

bound to a core hole. Excitons are characterized by their binding energy, which is related to their electron hole distance, or radius. Weakly bound excitons with a radius large in comparison to the lattice constant are known as Mott-Wannier [32, 33] excitons, shown in Fig. 1.9. More tightly bound excitons are known as Frenkel excitons [28] (not shown), which have a much smaller radius, comparable to the atomic lattice constant.

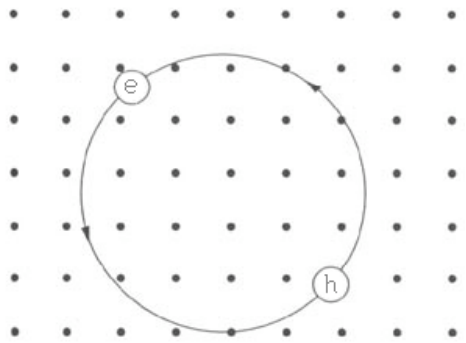

Fig. 1.9. An exciton is a bound electron-hole pair, which is free to move together through the crystal. Shown is a weakly bound, Mott-Wannier exciton, with an average electron hole distance large in comparison with a lattice constant [31].

1.4.3 Ionization Potential

The 1s ionization potential (IP) is the minimum energy required to excite a 1s electron to the continuum of states above the vacuum level. It is most conveniently measured by photoelectron spectroscopy (PES) as the difference between the exciting photon energy ħω and the kinetic energy of the photoelectron and work function of the material [27],

$$IP = E_B = h\nu_{exc} - E_{kin} - \Phi_{work} \qquad (1.2)$$

where E_B is the electron binding energy, $h\nu_{exc}$ is the energy of the exciting photon, E_{kin} is the kinetic energy of the photoelectron, and Φ_{work} is the work function of the material.

In carbon 1s → 2p absorption spectra, the 1s IP is characterized by a step-like increase in absorption intensity. Modeling the IP requires its energetic location, spectral shape and height to be considered, which are discussed in detail in Section 3.1.2 and Appendix A.1.

2 THEORY AND BACKGROUND

2.1 Bonding and Hybridization in Carbon

Understanding the hybridization (or overlap of orbital wavefunctions) of orbitals is important when discussing carbon systems. A neutral carbon atom has six electrons, which distribute themselves to fill the 1s and 2s subshells and the remaining two electrons occupy the 2p level, $1s^2 2s^2 2p_x^1 2p_y^1$. The basis of the hybrid orbitals is the excited configuration, $1s^2 2s^1 2p_x^1 2p_y^1 2p_z^1$, with four unpaired electrons. Four L-shell orbitals can then hybridize to form four new sp^3 orbitals, which are directed in tetrahedral directions at 109.5° angles (shown in Fig. 2.1, *right*). The K-shell remains unchanged. The primary bonding configuration in diamond is tetrahedral. Alternatively, the 2s and two of the 2p orbitals can hybridize to form three sp^2 orbitals, which are directed in trigonal directions at 120° angles from each other in a plane, as shown in Fig. 2.1, *left*. This is the primary bonding configuration in graphite or HOPG and C_{60}. The unused 2p orbital in sp^2 bonding lies perpendicular to the plane containing the three hybrid orbitals. In sp^1 (or sp) hybridization only one 2p orbital is used, resulting in digonal bonds 180° apart (Fig. 2.1, *bottom*). The two unused 2p orbitals in sp bonding lie perpendicular to the hybrid orbitals and each other. The unused 2p orbitals in sp^2 and sp^1 hybridization are free to form π bonds [27, 34]. Thus a measure of the amount of π bonding in a sample will measure the amount of sp^2 hybridization in it.

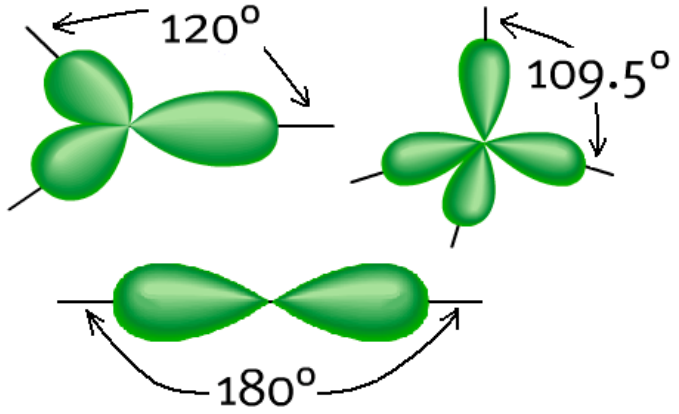

Fig. 2.1. ***Left*****: Three sp^2 hybrid orbitals formed by the combination of the 2s and two 2p orbitals; the unused 2p orbital lies perpendicular to the plane containing the hybrid orbitals.** ***Right:*** **Four sp^3 hybrid orbitals formed by the combination of the 2s and all three 2p orbitals.** ***Bottom:*** **Two sp^1 hybrid orbitals formed by the combination of the 2s and one 2p orbital; the two unused 2p orbitals lie perpendicular to the hybrid orbitals and to each other [35].**

2.2 C_{60}

2.2.1 Structure and Bonding of C_{60}

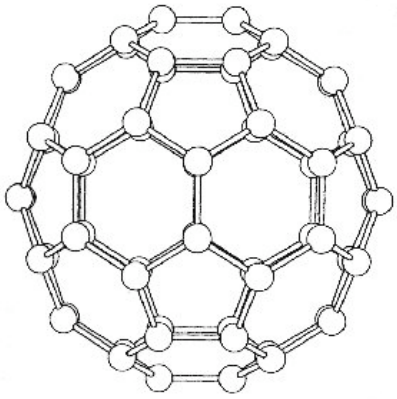

Fig. 2.2. Representation of the buckminsterfullerene (C_{60}) molecule [36].

Buckminsterfullerene, or C_{60}, consists of sixty carbon atoms on a sphere, whose surface has twenty hexagonal and twelve pentagonal faces (Fig. 2.2). Each atom in this configuration is the common corner to two hexagons and one pentagon so that,

of the three edges directed toward the neighbors, one is common to two hexagon edges and two are common to a pentagon and a hexagon [37, 38]. The angle between the σ and π orbitals is found to be 101.6°, and hence a σ bond may be considered to be inclined at an angle of 11.6° below a tangential plane to the surface. Nevertheless, C_{60} is found to have perfect π orbital overlap alignment, unlike most non-planar systems [39]. It is considered to be a fully sp^2 bonded 3-D π system [40].

2.2.2 Absorption of C_{60}

The XAS spectrum measured in TEY mode, as shown in Fig. 2.3, has four distinct features below 290 eV, which correspond to excitations into unoccupied π* bands. After the step-like increase in intensity at 290 eV, the features correspond to electronic transitions to unoccupied σ* bands and to the vacuum level. The XAS spectrum of C_{60} has been reproduced and reported by many people at various beamlines [38, 41 – 46]. Density of states (DOS) calculations confirm these assignments of features in the C_{60} absorption spectrum [47 – 52].

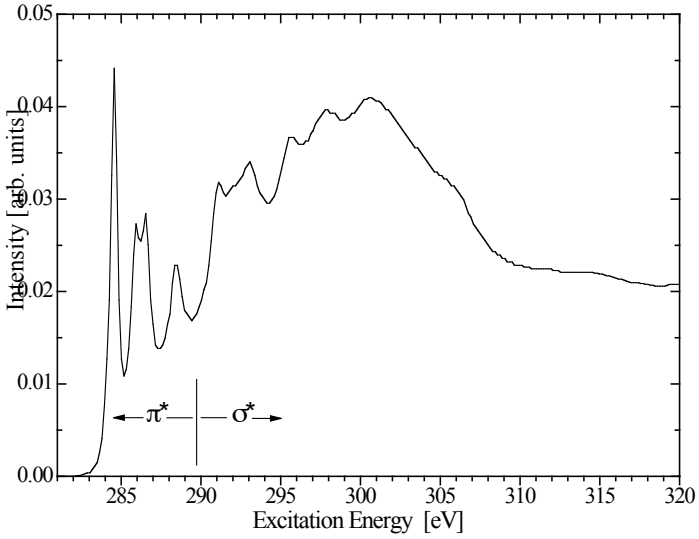

Fig. 2.3. C 1s absorption spectrum of C_{60}. The four features below 290 eV are due to electronic transitions to unoccupied π* bands; the features above are to unoccupied σ* bands and to the vacuum level.

Since the C_{60} molecules interact only weakly (via van der Waals interaction) with one another, the spectroscopic data are expected to predominately reflect the electronic and geometric structure of the individual molecules [38]. This is important since the calculational models consider only the structure of a single molecule, but are used here to accurately reflect measured spectra of C_{60} in powder form.

2.2.3 Oxygen-C_{60}

It is also important to consider possible sample contamination, such as an oxygen-C_{60} compound. T. Kaambre *et al.* [53] investigated UV light-induced oxidation of C_{60}, in which oxygen has been shown to adsorb to the surface and intercalate readily into the interstitial sites in the C_{60} lattice after many hours of UV light exposure [54, 55], resulting in an approximately $C_{60}O_1$ stoichiometry in the bulk of the sample. Absorption spectra of an oxygen-C_{60} compound and of pristine C_{60} (Fig. 2.4) show subtle differences in absorption intensity, but relative to the C_{60} spectrum, the $C_{60}O_x$ spectrum is broadened. Convolving the C_{60} spectrum in Fig. 2.4 with a 0.35 eV FWHM Gaussian gives a close fit to the $C_{60}O_x$ spectrum [53]. One would then expect differences in the weighting of π^* to total integrated area of these spectra would be relatively small. Taylor *et al.* [56] conclude that C_{60} may be ultraviolet sensitive in the absence of oxygen, and may partly decompose under exposure. Further, samples of C_{60} should be stored in the dark under vacuum or nitrogen. However, the C_{60} samples used in our experiment are kept in a dark container, but not under vacuum, until a small amount is removed for measurement. The UV exposure time of our C_{60} samples is much lower than those in Kaambre's experiments, so it is expected that the oxygenation is much less, and thus the spectral differences will be negligible. Our samples are not stored under vacuum and have not been compared to pristine C_{60}.

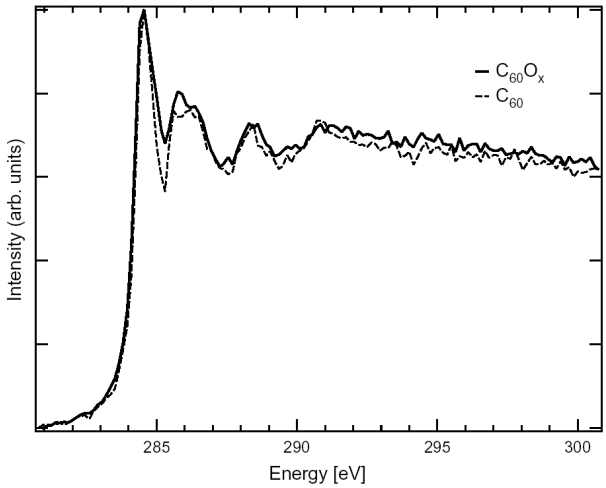

Fig. 2.4. XAS spectra of C_{60} and $C_{60}O_x$, measured in TFY mode [53].

2.3 Highly Oriented Pyrolytic Graphite (HOPG)

2.3.1 Structure and Bonding of Highly Oriented Pyrolytic Graphite

The principal structure of highly oriented pyrolytic graphite (HOPG), shown in Fig. 2.5, consists of layers of carbon atoms in an sp^2 bonding configuration. Each layer is considered a basal plane. Carbon atoms within a single plane interact much stronger than with those from adjacent planes [57]. All the atoms are sp^2 hybridized; each atom is covalently bonded to three other atoms. The remaining unhybridized $2p_z$ orbital is free to form a π bond. Because of their similar shape and orientation, each $2p_z$ orbital overlaps two others, one on each adjacent carbon atom, to form delocalized molecular orbitals, which are not confined between two adjacent bonding atoms. Therefore, electrons are free to move around this extensively delocalized molecular orbital making HOPG a good conductor of electricity in directions along the planes of carbon atoms [58].

Each carbon atom within a plane of HOPG has three nearest neighbors, resulting in a honeycomb structure. The adjacent layers are offset as shown in Fig. 2.5, so that even-numbered layers lie directly below each other, and odd-numbered layers lie

directly below each other in an alternating pattern. Adjacent planes are weakly attached, thus small sheer stresses can easily separate them. HOPG atoms are fully sp^2 hybridized, similar to C_{60}. The σ orbitals lie in the basal plane, and π orbitals lie perpendicular to it [59, 60].

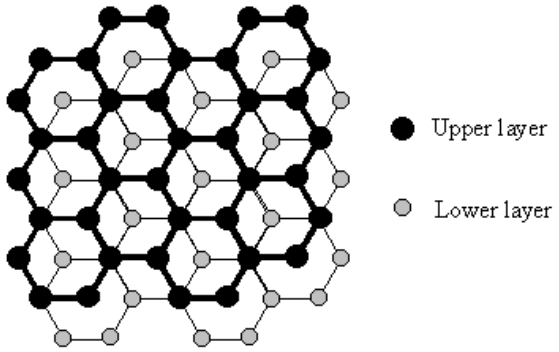

Fig. 2.5. Two layers of HOPG's honeycomb structure [57]. Each layer is considered a basal plane.

2.3.2 Absorption of HOPG

X-ray absorption spectra of HOPG are characteristic in their features. The strong low energy structure at 285.5 eV is due to electronic transitions from the 1s level to unoccupied π* bands, as shown in Fig. 2.6. This corresponds to a physically out of plane bond. Features above 292 eV are due to transitions from the 1s level to unoccupied σ* bands and to the continuum [43, 60 – 64]. The sharp feature at 292 eV is not due to the conduction band structure, but to a core excitonic state (Frenkel) [43, 60].

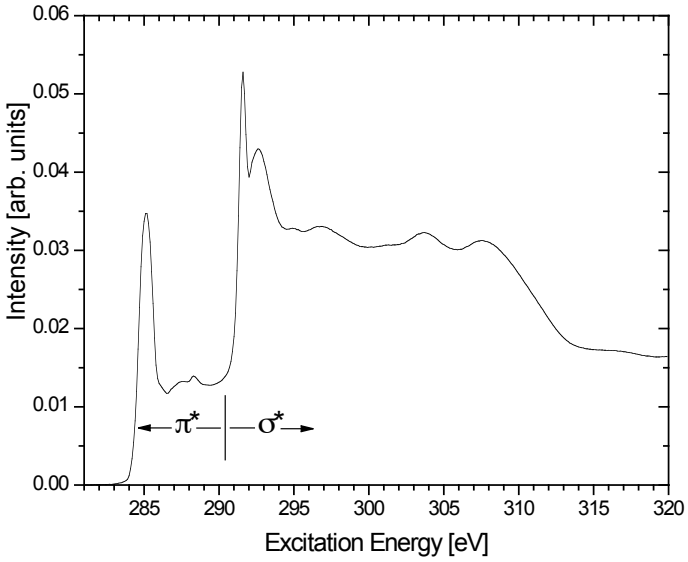

Fig. 2.6. Soft x-ray absorption spectrum of HOPG. Features below 290 eV are due to electronic transitions to unoccupied π* bands; above is to unoccupied σ* bands and to the continuum.

2.3.3 Angular Dependence of HOPG Absorption Spectra

Incident rays normal to the basal plane of graphite do not efficiently excite 1s electrons to the π* band. Similarly, grazing rays do not efficiently excite the σ* bands [59 – 61]. Normal incident radiation couples with in plane σ* orbitals, and grazing radiation couples with out of plane π* orbitals (Fig. 2.7). Coupling occurs when the electric field vector, which is perpendicular to the incoming rays, is parallel to the orbital's orientation. Since the absorption spectrum exhibits both π* and σ* features, relative intensities also have a dependence on incidence angle. The low energy π* features are greatly diminished at normal incidence, and the high energy σ* features are enhanced. The reverse is true at grazing incidence. This does not, however, affect the energetic locations of the features, only their intensities.

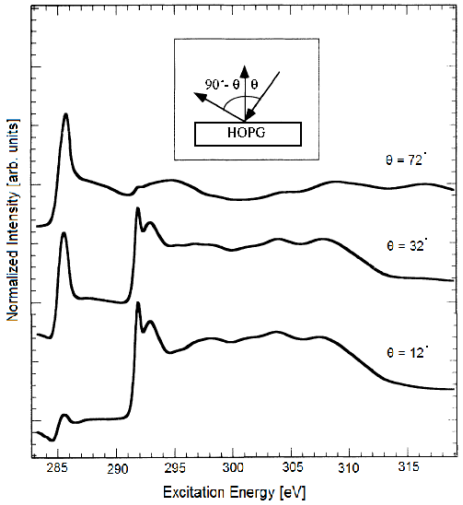

Fig. 2.7. Angular dependence of HOPG absorption spectrum [65].

2.3.4 Excitation Energy Scale Calibration

During a series of measurements, the monochromator grating is physically rotated to select different excitation energies. After repeated movements of the monochromator it will not return exactly to its original position due to backlash in the grating rotational motion. The main purpose of HOPG in this study is to provide an energy scale calibration for all carbon spectra. Carbon 1s → 2p absorption spectra are always accompanied by a measurement of HOPG. Afterwards, all energy scales are shifted the same amount so that the π* resonance of HOPG is located at 285.5 eV. Table 2.1 shows general agreement among researchers of the energetic location of the π* feature in HOPG, within 1 eV.

Table 2.1. Locations of the π* feature in HOPG in various papers.

π* (eV)	285.5	285.4	285.3	285	285.2	286	285	285	285.5
Ref.	64	61	22	43	66	59	67	68	69

2.4 Diamond

2.4.1 Structure and Bonding of Diamond

Diamond, an allotrope of carbon, is the hardest natural material. Each carbon atom is sp^3 hybridized, and bonded to four other atoms in a tetrahedral formation, as shown in Fig. 2.8. This covalent network of bonding in three dimensions contributes to diamond's hardness [58].

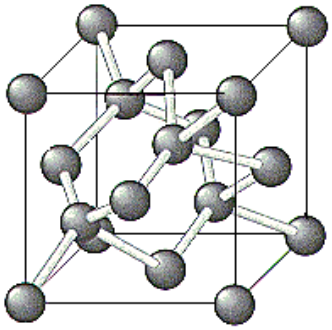

Fig. 2.8. Covalent bonding structure of diamond [70].

2.4.2 Absorption of Diamond

Since all of the 2p orbitals in fully sp^3 hybridized materials are used, there are no unoccupied π^* orbitals. Thus, pure diamond will not exhibit any π^* features in absorption spectroscopy (Fig. 2.9). This absorption spectrum is typical, and has been reproduced by many other groups [60, 71 – 76]. The sharp feature at 289.5 eV is excitonic in nature [66, 71, 72, 76 – 78], and features higher in energy than that are due to electronic transitions from the 1s core level to σ^* bands and to the continuum. In impure diamond or nanodiamond, π^* features located at 285.5 eV will begin to appear [79 – 83]. These are unused 2p orbitals resulting from sp^2 hybridization, which are free to form π bonds. Some π bonding is even expected in pure diamond due to structural differences between its surface and bulk; the tetrahedral network of bonds must be discontinued at the surface [84]. The intensity

of that feature increases with impurity. Other than the low energy π* feature of nanodiamond, pure diamond and nanodiamond are spectroscopically nearly the same.

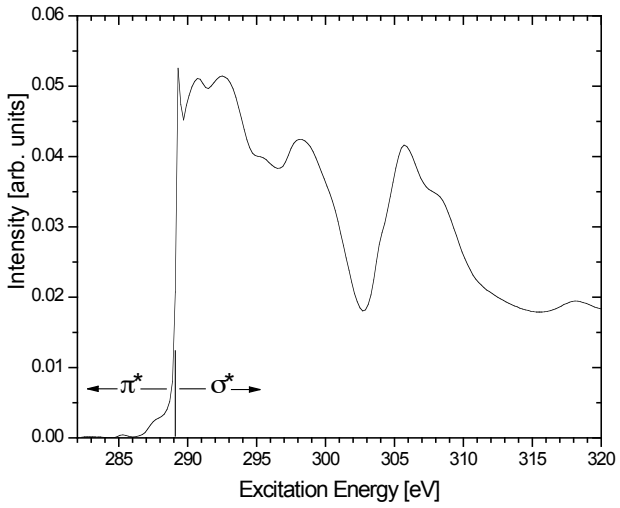

Fig. 2.9. C 1s absorption spectrum of diamond. The sharp excitonic feature at 289.5 eV separates π* (lower energy) and σ* (higher energy) resonances.

2.4.3 Nanodiamond

Nanodiamond films are clusters of diamond-structured carbon grown on treated silicon substrates by hot filament chemical vapour deposition in a CH_4/H_2 gas mixture [85]. Depending on conditions of the substrate and atmosphere, diamond grows in small clusters. Cluster sizes are typically 2 nm in diameter. As mentioned in Section 2.4.2, nanodiamond films are expected to exhibit a π* resonance at 285.5 eV due to the discontinuity at the boundary of each cluster. The intensity of the π* resonance, thus sp^2 concentration, varies with nanodiamond grain size [81].

2.5 Amorphous Carbon

2.5.1 Structure and Bonding of Amorphous Carbon

An amorphous solid is one that exhibits no crystalline structure or long-range order. It only possesses a short-range order in the sense that the nearest neighbours of an atom are well defined by virtue of chemical bonding requirements [34]. Amorphous carbon (a-C) holds true to this nature; it lacks the crystalline order of diamond or HOPG. In a sense, one could think of amorphous carbon as having a mixture of diamond (sp^3) and HOPG (sp^2) bonding characteristics. a-C should not be thought of as one specific sample, but as a category of samples, unlike diamond, HOPG and C_{60} because of various mixtures of sp^2 and sp^3 bonding.

Carbon atoms in a-C films are sp^2 and sp^3 hybridized, with no sp^1 hybridization. Significant sp^1 bonding would give rise to a σ^* feature at 310 eV, which is not seen in any a-C film, [67] including the spectra presented in this study. Therefore, the concentration of sp^1-bonded atoms is considered negligible in a-C films.

2.5.2 Absorption of Amorphous Carbon

Several computer simulations of a-C have been carried out [86 – 90] in order to gain insight into its structure and absorption spectrum. These studies report various amounts of sp^2 hybridization, but suggest that π^* resonances are expected up to approximately 4.5 eV above the initial onset of C 1s $\rightarrow$ 2p absorption. For the a-C samples in this study, features below and including 288.5 eV will be labeled π^* resonances, which is in accordance with several papers studying carbon films [75, 91 – 93]. Shown in Fig. 2.10 is the absorption spectrum of an amorphous carbon tape. Spectra of other a-C films may vary in fine structure, but all will have the characteristic π^* resonance at 285.5 eV.

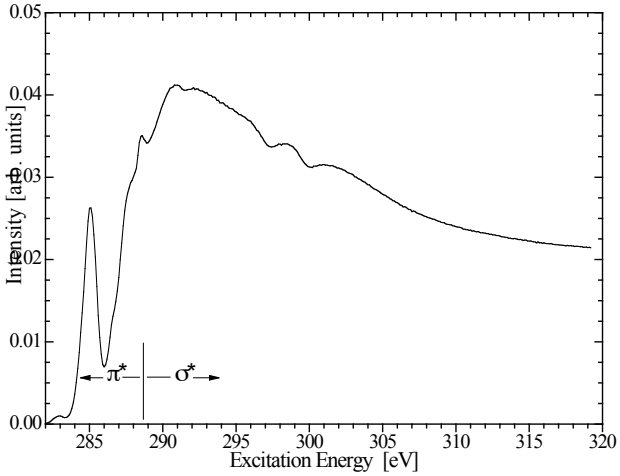

Fig. 2.10. C 1s absorption spectrum of amorphous carbon tape.

2.6 Spectroscopic Analysis of Carbon Films

A chemical characterization of a-C that serves to associate its electronic structure with its physical properties is important to the development of customizable a-C films. Several measurement techniques with varying success have been used to determine the sp^2 bonding concentration of a-C films, such as Auger electron spectroscopy (AES), Raman spectroscopy, x-ray photoemission spectroscopy (XPS), electron energy loss spectroscopy (EELS), and x-ray absorption spectroscopy (XAS). These techniques probe the electronic structure of carbon to reveal differences in their sp^2 and sp^3 characteristic. Analyses vary by technique, and are discussed in the following sections.

2.6.1 Raman Spectroscopy

Raman spectroscopy measures the wavelength and intensity of inelastically scattered light from atoms or molecules. The scattered light occurs at wavelengths that are shifted from the incident light by inelastic losses due to the molecular vibrations. The energy difference between the incident photon and the Raman scattered photon is equal to the energy of the vibration. Using a monochromatic and

high-intensity light source, such as a laser, the energy shifts can be easily detected. Materials with characteristic vibrations can be identified using this technique. Studies using Raman spectroscopy [94, 95] deconvolve the spectra by superimposing peaks positioned at wavenumbers associated with diamond (sp^3) and graphite (sp^2) features. A trend in sp^2 concentrations of a-C films can be shown using the relative integral intensities of their fitted diamond and graphite peaks. Absolute values of sp^2 are unavailable because no reference is used. There is also significant peak overlap in these spectra, which leads to ambiguity in selecting fitted peak widths and locations.

2.6.2 Auger Electron Spectroscopy

When a sample is bombarded with x-rays or electrons and a core hole is produced, the atom will relax via Auger emission of an electron or fluorescence emission (Section 1.3). The energy given off by an electron refilling the core hole in the Auger process is transferred to another electron, which is ejected from the sample. This leaves two new holes in the sample. For example, if a K-shell hole is created, an L_1-shell electron may annihilate the core hole, transferring its energy to an $L_{2,3}$-shell electron, which is then ejected from the sample. The transition is labeled KLL. Auger electron spectroscopy (AES) is a technique that detects the characteristic kinetic energies of these emitted electrons. Auger electron kinetic energies are not dependant on incoming photon energy. Each material will exhibit a characteristic spectrum with features of various intensities at different kinetic energies. In order to determine the sp^2 bonding concentration of a-C films, researchers evaluate peak shapes of the KVV transitions involving π electrons [96 – 98]. This allows only estimations of the sp^2 bonding concentrations of samples due to the lower resolution spectra.

2.6.3 X-Ray Photoemission Spectroscopy

X-ray photoemission spectroscopy (XPS) is based on the photoelectric effect, and probes the occupancy of core and valence electrons in a material. When incoming x-rays of sufficient energy excite a sample, a core or valence electron may be ejected. The kinetic energy of this photoelectron is given in Equation 1.2. Measured spectra are typically displayed on the binding energy scale, where $E_B = 0$ at E_F, the Fermi level. Intensities of core level peaks are directly proportional to the density of atoms. Since XPS is an electron detecting technique, it is surface sensitive, similar to TEY absorption (Section 1.2.1). Photoelectron line energies are dependant on the incoming photon energy. Great detail on XPS can be found in Ref. [99].

Since the C 1s core level binding energies of sp^2 and sp^3 hybridized orbitals are different, the C 1s photoemission spectra are decomposed into two lines. Separation of the fitted sp^2 and sp^3 peaks remains constant and is equal to the separation of the core level binding energies of graphite and diamond [100]. The relative integrated intensity of the sp^3 peak is used as the measure of the amount of sp^3 bonding in the material. Other research [96, 101 – 103] follows a similar method. This technique relies on the assumption that sp^2 and sp^3 peaks in a-C XPS spectra will appear at the same binding energy as for graphite and diamond, respectively. The C 1s XPS spectra also appear as essentially one wide feature, such that unambiguously fitting the sp^2 and sp^3 peaks becomes difficult. This introduces large error into the sp^3 concentration determinations, where only a rough estimation is possible.

2.6.4 Electron Energy Loss Spectroscopy

Electron energy loss spectroscopy (EELS) involves bombarding a sample with a beam of mono-energetic electrons and detecting the inelastically scattered electrons' kinetic energies. In the low-loss region (<100 eV), electrons induce plasmon oscillations. In the high-loss region (>100 eV), energy from the incident electron is transferred to inner-shell electrons, which are then ejected from the sample. These losses of energy are characteristic of the binding energies of different

elements, and so EELS spectra closely resemble XAS (1.2) spectra, but with typically lower resolving power.

Berger *et al.* [104] devised a method of analyzing EELS spectra to determine an a-C film's sp^3 concentration, which is linked to its hardness. The intensity of the π* resonance in EELS spectra of a-C is used to ascertain the concentration of π bonded atoms in the films, because the absorption intensity of the electronic transitions from the C 1s core level to the π* antibonding states should be proportional to the concentration of sp^2 bonded atoms [1]. The integral area of the C 1s → π* transitions in the carbon K-edge of a film, $I_{u\pi^*}$, normalized to the total integral area, $I_u(\Delta E)$, gives a number which is proportional to the number to π bonded electrons in that material. This number, $I_{ref\pi^*}/I_{ref}(\Delta E)$, in a sample of known 100% sp^2 bonding thus represents 100% sp^2 bonding. Therefore, the concentration of sp^2 bonded atoms in a carbon film can be determined from the ratio of the π* peak integral in the film to that of the reference given by

$$sp^2\% = \frac{I_{u\pi^*}}{I_{ref\pi^*}} \frac{I_{ref}(\Delta E)}{I_u(\Delta E)} 100\%, \qquad (3.2)$$

where $I_u(\Delta E)$ and $I_{ref}(\Delta E)$ are the integrated counts over some energy window ΔE [104]. This leads to several variations and applications of the method using EELS [68, 105 – 109].

2.6.5 X-Ray Absorption Spectroscopy

Many researchers [1, 60, 67, 75, 92] have applied the technique described in the previous sections instead to XAS spectra of a-C films. The added benefit of employing XAS over EELS is the opportunity of increased spectral resolution. The XAS spectra used in this study show much more detail and have much higher resolution than EELS spectra. Information can be lost in the lower resolution EELS spectra, where XAS spectra do not suffer. In addition, XAS spectra of a-C have

better separation of π^* and σ^* features, where in EELS spectra there is significant overlap of the features. Significant overlap increases the error involved due to increased ambiguity when fitting both π^* and σ^* features.

Careful examination and labeling of the π^* features in both the reference and unknown samples in XAS spectra are crucial in order to accurately represent the sp^2 concentrations of the unknown samples.

3 ANALYSIS

3.1 Revised Method

Considering all previous methods of determining the sp^2 concentration of a film, a revised model has been developed. This new method addresses many of the problems and differences in past methods that have arisen, and relies on the superior XAS measurement technique. The following subsections outline the steps involved in the revised method for determining the sp^2 concentrations in carbon films.

3.1.1 Reference Sample

Past studies have used HOPG and C_{60}, among others, as reference standard samples. Both of these materials have a well defined and studied structure with 100% sp^2 bonding. Díaz *et al.* [1], Papworth *et al.* [68], and Gago *et al.* [69] recommend against using HOPG as a reference sample in a-C film sp^2 characterization due to the orientation effects of HOPG absorption spectra (2.3.3) and crystal structure. C_{60}, however, makes an excellent reference sample because it is fully sp^2 hybridized, has a well-identified π^* structure [1], and lacks orientation-dependant absorption.

3.1.2 Ionization Potential Considerations

Some of the methods discussed previously dismiss the ionization potential when fitting spectra, or, if it is considered, implement it differently than here. The location of the edge jump of the 1s ionization potential is chosen to be where the energy of incoming photons is first able to promote 1s electrons to the continuum

states. Depending on the carbon allotrope, this occurs around 289 – 290 eV [1, 110, 111].

The onset is modeled with a Heaviside-step convoluted with a Lorentzian function of 1 eV width [112] to give a smooth increase. After the initial increase, an exponential decay is applied to accurately model the absorption cross section of carbon. The decay matches that of the absorption cross-section of bulk carbon [19]. The ionization potential's height is chosen such that it matches the spectral height between the 320 – 340 eV extended region, but does not exceed it at any point [1]. This is the first method to implement an exponential decay, where others have assumed constant height above the step. Fig. 3.1 demonstrates the differences between fitting to an XAS spectrum ionization potentials with a constant height above the onset and with an exponential decay applied above the onset.

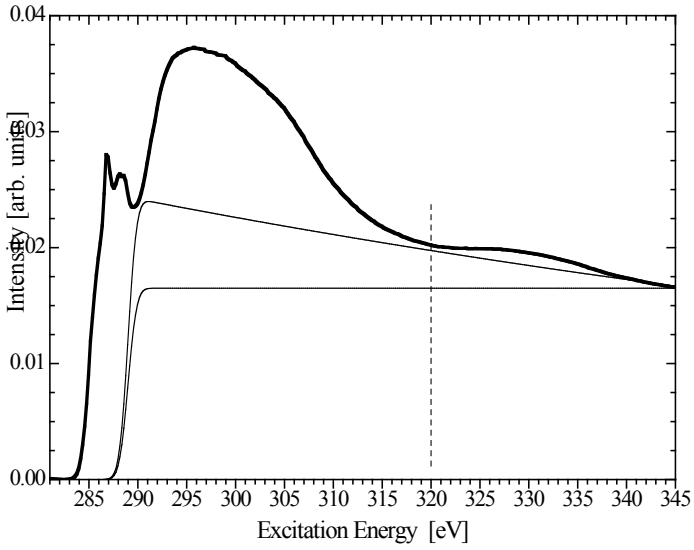

Fig. 3.1. C 1s absorption of an a-C film fitted with constant height above onset and exponentially decaying ionization potentials. Total area integration for all carbon XAS spectra is over 280 – 320 eV.

In most previous models, absorption is measured at most from 280 – 320 eV and total area integration is over that same range. It is apparent from Fig. 3.1 that if

absorption is only measured up to 320 eV, then the decrease of IP can not be properly determined. Using a constant height IP and having measured up to only 320 eV, one would chose the ionization potential's height to match the absorption intensity of a-C at 320 eV, which would then exceed the actual absorption over 320 eV. Decay of the absorption cross section from Henke *et al.* [19] applied to the step function IP results in a fit that closely follows the gradual decline of the a-C film absorption. The decaying IP is essential to correctly model the high energy region in a-C. It is expected that there are no σ* features above 320 eV in a-C, only a multielectron transition at 330 eV [67]. As seen in Fig. 3.1, the decaying IP coincides with absorption intensity and eliminates the necessity of fitting unrealistic high-energy σ* peaks, but the constant height IP does not. Further discussion on the ionization potential fitting function is found in Appendix A.1.

3.1.3 π* Identification

Correct characterization of π* features in XAS spectra allows accurate determinations of the sp^2 concentrations in a-C and nanodiamond films. π* features in the XAS spectra of C_{60}, HOPG, diamond, and a-C (Fig. 3.2) are designated according the discussions in sections 2.2.2, 2.3.2, 2.4.2, and 2.5.2, respectively.

There has not been complete agreement among previous researchers on the labeling of π* features in a-C films, possibly due to the wide variety of a-C structures possible. Based on several model calculations [86 – 90] and previous π* assignments [75, 91 – 93], the π* to σ* cut-off boundary in a-C occurs around 288.5 eV. Features centered below that cut-off point are then π*; above are σ*. This fitting model can then be applied to all carbon allotropes, provided the π* features in the absorption spectra are correctly identified.

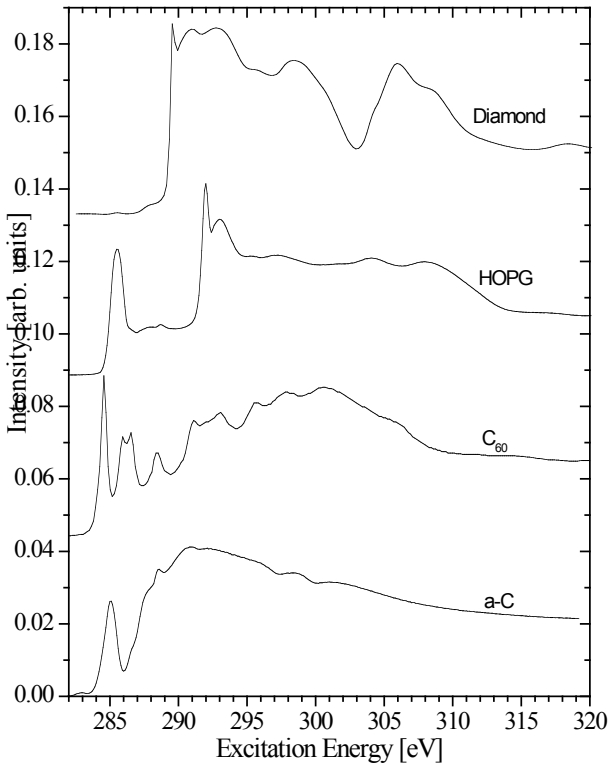

Fig. 3.2. C 1s absorption spectra of, from top to bottom, diamond, HOPG, C_{60}, and a-C.

3.1.4 Gaussian Fitting of π* and σ* Features

Before any analysis of the XAS spectrum is made, the background is subtracted in order to recover the primary spectrum. Each spectrum is matched at the pre-edge (below the 1s → 2p onset) to a constant height background, which is then subtracted. More specifically, the minimum height of the spectrum is set to zero by subtracting equally the background from the whole spectrum. This instrumental background does not contribute useful information for analysis. An ionization potential is then fitted to the background-subtracted XAS spectrum and it too is subtracted, leaving a difference spectrum representing only the contributions of π* and σ* features to the primary spectrum. It is this portion of the spectrum that is analyzed, and is called the subtracted spectrum.

Symmetrical Gaussian functions are used to fit the π* and σ* features in the subtracted spectra. The heights, widths and energetic positions of the Gaussians (Appendix A.2) are controlled with OriginLab™ Origin® scientific graphing and analysis software. The minimum number of Gaussian functions is used to fit each spectrum, determined by attempting to create complete agreement between the subtracted spectrum and the sum of the fitted Gaussians with progressively fewer peaks. When complete agreement is not met, one too few peaks is selected. Energetic positions of π* Gaussians are chosen to lie below the π* to σ* cut-off boundary, and coincide with peak features in the subtracted spectrum. Positions of σ* Gaussians, on the other hand, lie above the cut-off boundary.

Each fitted Gaussian peak corresponds to a C 1s → π* or σ* transition in the sample, depending on energy position. Heights and widths resemble spectral heights and broadening, respectively.

3.1.5 Integration Energy Window

The 280 – 320 eV total intensity integration window is selected for a variety of reasons. Berger *et al.* [104] calculated the sp^2 concentration of amorphous carbon while varying the energy window size from 20 – 120 eV, starting from 280 eV. The sp^2 concentration steadily increased by only 4%. A 40 eV (280 – 320 eV) window is used in here in accordance with [1], which avoids having to model the multi-electron transition at 330 eV in a-C [67]. The intensity of this feature [113] requires further calculation, which can be avoided with its exclusion from the total area integration.

3.2 a-C films Deposited on PTFE Substrates

3.2.1 a-C Film Preparation

The amorphous carbon films are deposited onto a 100 μm thick polytetrafluoroethylene (PTFE) substrate in a DC glow discharge plasma in which a graphite target is sputtered. The concentration of nitrogen in the atmosphere is varied from 0 – 20%. The deposition results in a 220 nm thick carbon film. Details of the film deposition can be found in [7].

3.2.2 C 1s Absorption of a-C Films on PTFE Substrates

Total electron yield (TEY) absorption measurements of the PTFE substrate a-C films were taken at the C 1s → 2p (CB) edge (Fig. 3.3) at beamline 8.0.1 of the ALS. Spectral fits, shown in Fig. 3.4 – Fig. 3.8 are then performed according to the method previously outlined in Section 3.1, and the Gaussian fitting parameters of the π^* features are listed in Table D.2.

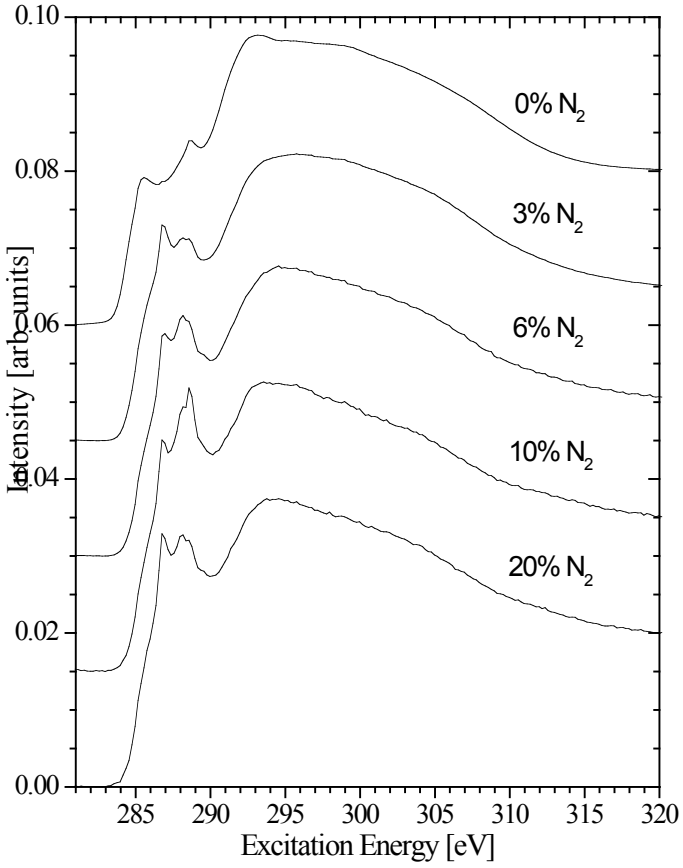

Fig. 3.3. C 1s absorption spectra of a-C films deposited on PTFE substrates in increasing N_2 atmospheres (top to bottom).

A change in the electronic structure of a-C occurs when nitrogen is introduced in the atmosphere during deposition. The films deposited in non-zero nitrogen atmospheres have very similar structure, with features at the same energetic locations; only their relative intensities change. The lowest energy π^* feature in the C 1s absorption spectrum of 0% N_2 film appears at a lower energy than spectra of the rest of the films.

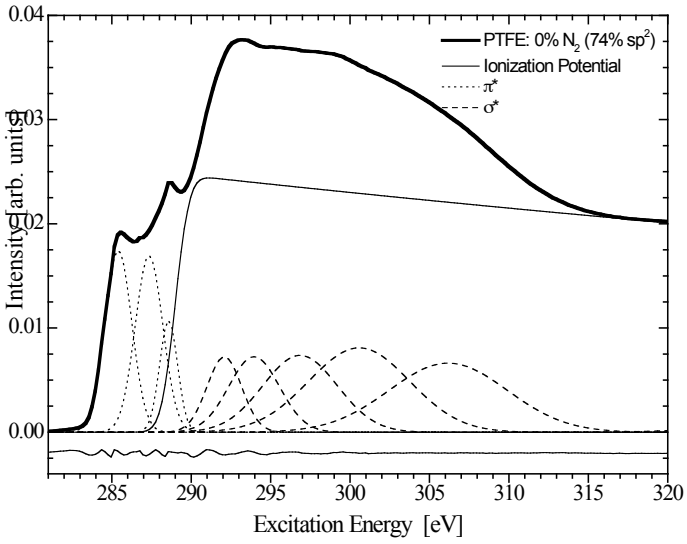

Fig. 3.4. Fitted C 1s absorption spectrum of a-C film deposited on a PTFE substrate in a 0% N_2 atmosphere resulting in a 74% ± 5% sp^2 concentration. Line underneath is difference between experimental data and fitting curve.

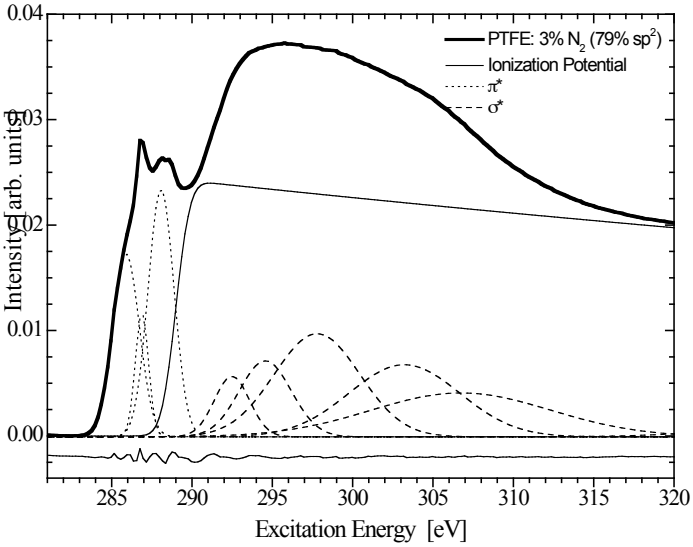

Fig. 3.5. Fitted C 1s absorption spectrum of a-C film deposited on a PTFE substrate in a 3% N_2 atmosphere resulting in a 79% ± 5% sp^2 concentration. Line underneath is difference between experimental data and fitting curve.

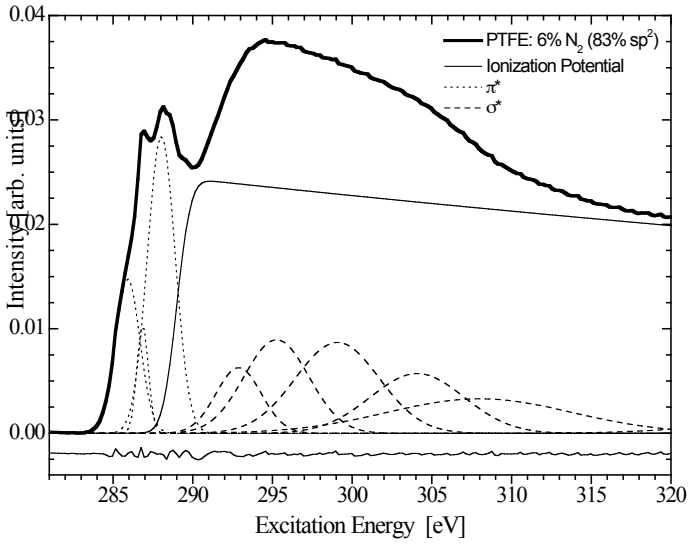

Fig. 3.6. Fitted C 1s absorption spectrum of a-C film deposited on a PTFE substrate in a 6% N_2 atmosphere resulting in a 83% ± 5% sp^2 concentration. Line underneath is difference between experimental data and fitting curve.

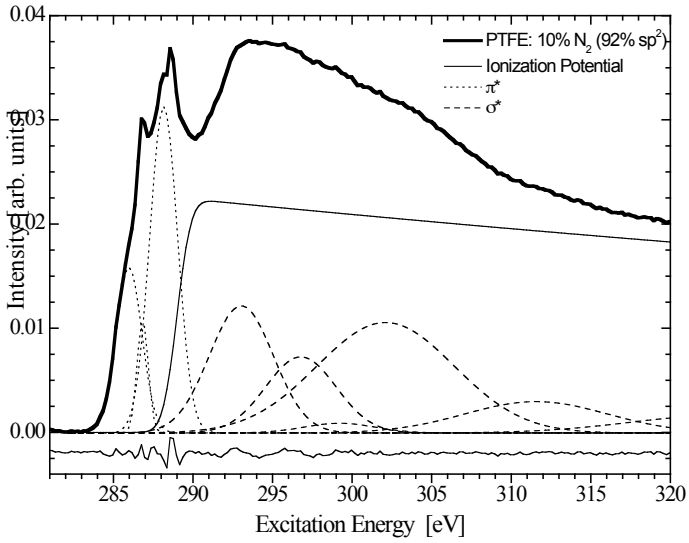

Fig. 3.7. Fitted C 1s absorption spectrum of a-C film deposited on a PTFE substrate in a 10% N_2 atmosphere resulting in a 92% ± 5% sp^2 concentration. Line underneath is difference between experimental data and fitting curve.

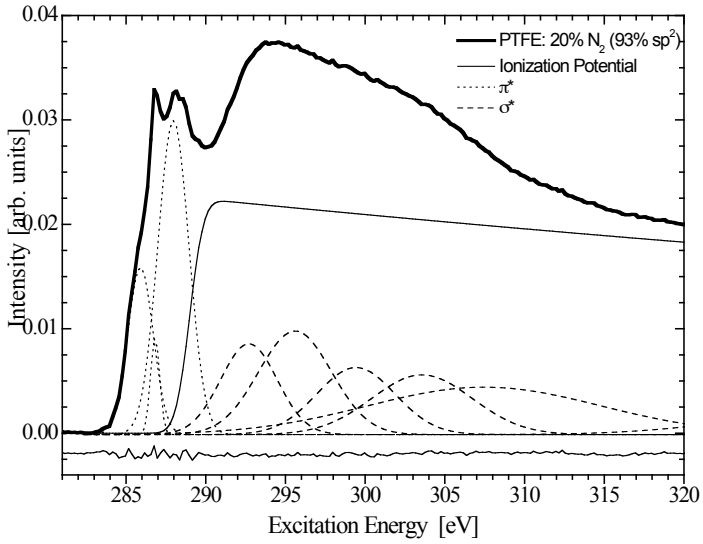

Fig. 3.8. Fitted C 1s absorption spectrum of a-C film deposited on a PTFE substrate in a 20% N_2 atmosphere resulting in a 93% ± 5% sp^2 concentration. Line underneath is difference between experimental data and fitting curve.

As the N_2 atmosphere is increased, sp^2 bonding concentrations in these films increases from 74 – 93% ± 5% (Fig. 3.9). Please refer to Appendix B for discussion on error determination. This rise in sp^2 concentration is in accordance with other studies on nitrogenated a-C films [68, 92, 108, 114, 115]. There is a detectable change in electronic structure of the carbon atoms when nitrogen is introduced. It appears that increasing the nitrogen atmosphere above 10% during deposition does not further increase the sp^2 concentration in the films; a saturation of sp^2 bonding is reached. The limit of sp^2 bonding is 92% ± 5%, achieved during deposition in a 10% N_2 atmosphere.

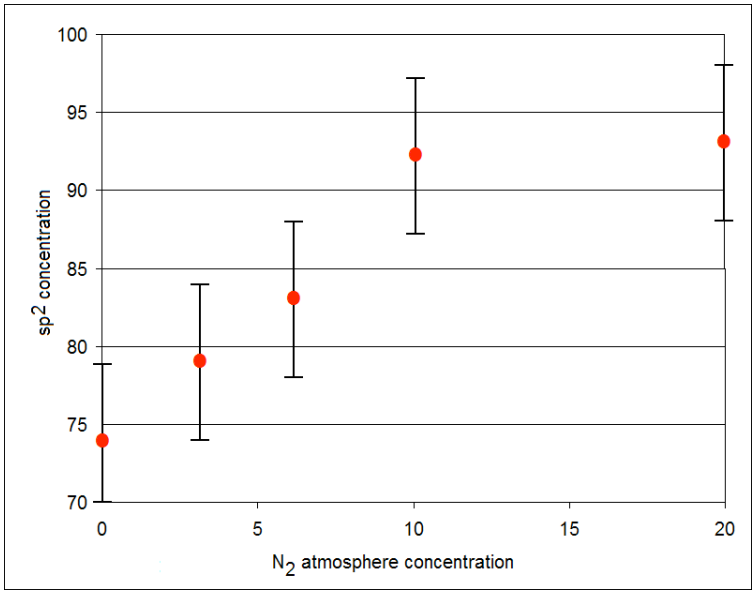

Fig. 3.9. Concentration of sp^2 bonding experimentally determined for a-C films deposited on PTFE substrates.

An adjustment of the π* peak positions occurs when increasing the N_2 atmosphere during deposition from 0% to 3%, where they remain stable upon higher N_2 doping (see Table D.2). Interestingly, the onset π* peak lies 0.5 eV lower in the 0% N_2 film than in the others. That π* orbital is then more heavily influenced by the core level without nitrogen doping. Between the films, the two higher energy fitted π* features exhibit little correlation in terms of their spectral heights and widths.

3.2.3 Kα XES of a-C Films on PTFE Substrates

Carbon Kα (2p → 1s) x-ray emission spectroscopy (XES) spectra of a-C films deposited on PTFE substrates (Fig. 3.10) show that there is essentially no difference between XES spectra in the films deposited in 3 – 20% N_2 atmosphere. There is a small difference, however, in intensity at 277.5 eV between the films deposited in a nitrogen atmosphere and the film without. We conclude that nitrogen incorporation into the carbon film slightly changes the occupied 2p carbon states. Increasing the nitrogen atmosphere above 3% does not have any further effect on this.

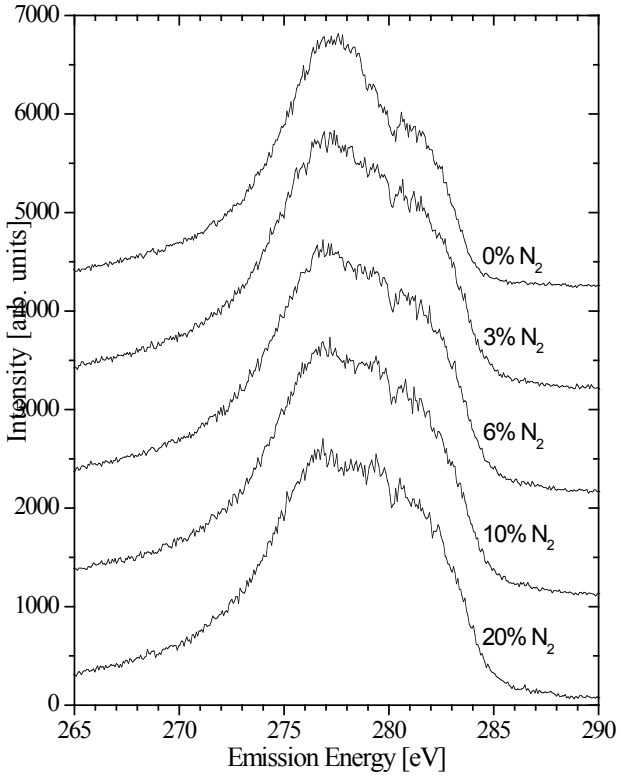

Fig. 3.10. Kα XES spectra of a-C films deposited on PTFE substrates in increasing N_2 atmospheres (top to bottom).

3.3 a-C Films Deposited on Silicon Substrates

3.3.1 a-C Film Preparation

Films are deposited simultaneously onto PTFE (Section 3.2.1) and silicon substrates under the same conditions to minimize variation between these films on different substrates.

3.3.2 C 1s Absorption of a-C Films on Silicon Substrate

The same measurement technique and analysis were applied to these samples as the PTFE substrate a-C films (Section 3.2.2). Measured XAS spectra of the silicon

substrate a-C films are shown in Fig. 3.11, and fits in Fig. 3.12 – Fig. 3.16. sp^2 bonding concentrations in these films vary from 82 to 89% ± 5% (Fig. 3.17).

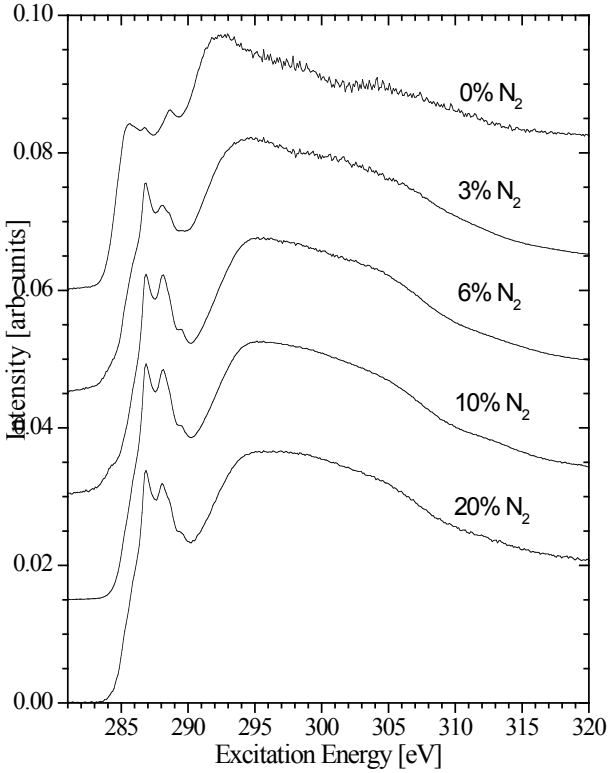

Fig. 3.11. C 1s absorption spectra of a-C films deposited on silicon wafer substrates in increasing N_2 atmospheres (from top to bottom).

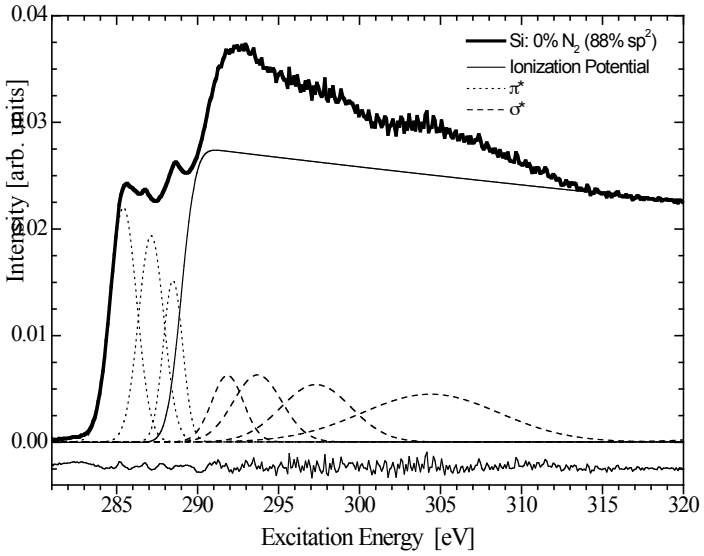

Fig. 3.12. Fitted C 1s absorption spectrum of a-C film deposited on a silicon substrate in a 0% N_2 atmosphere resulting in a 88% ± 5% sp^2 concentration. Line underneath is difference between experimental data and fitting curve.

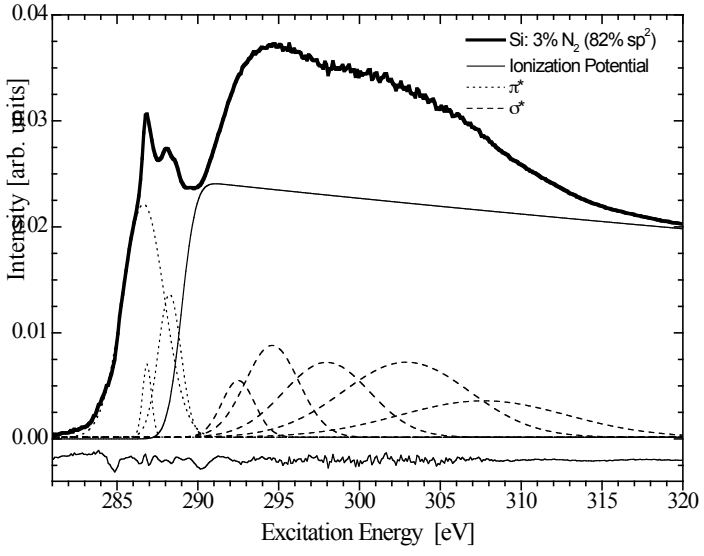

Fig. 3.13. Fitted C 1s absorption spectrum of a-C film deposited on a silicon substrate in a 3% N_2 atmosphere resulting in a 82% ± 5% sp^2 concentration. Line underneath is difference between experimental data and fitting curve.

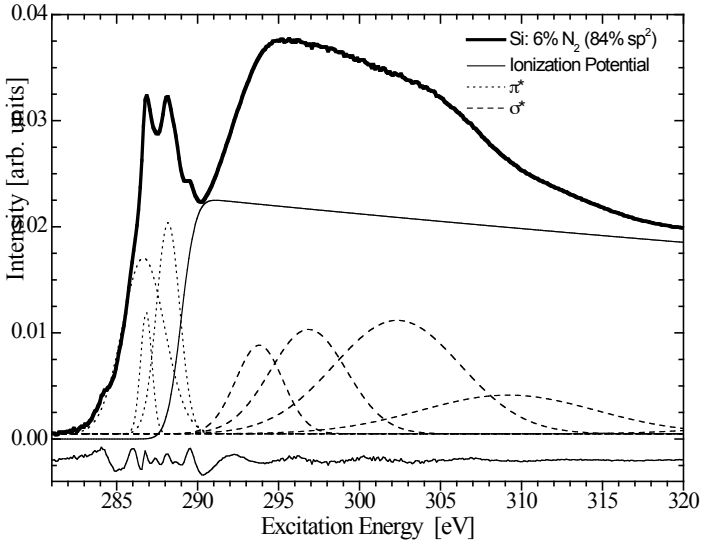

Fig. 3.14. Fitted C 1s absorption spectrum of a-C film deposited on a silicon substrate in a 6% N_2 atmosphere resulting in a 84% ± 5% sp^2 concentration. Line underneath is difference between experimental data and fitting curve.

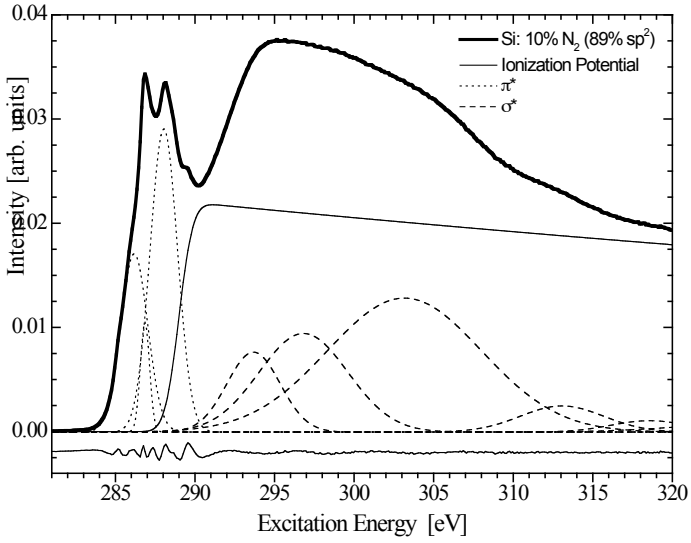

Fig. 3.15. Fitted C 1s absorption spectrum of a-C film deposited on a silicon substrate in a 10% N_2 atmosphere resulting in a 89% ± 5% sp^2 concentration. Line underneath is difference between experimental data and fitting curve.

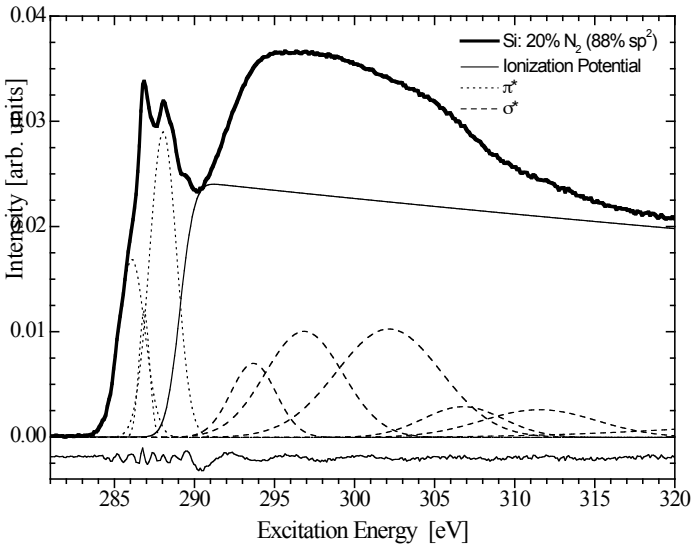

Fig. 3.16. Fitted C 1s absorption spectrum of a-C film deposited on a silicon substrate in a 20% N_2 atmosphere resulting in a 88% ± 5% sp^2 concentration. Line underneath is difference between experimental data and fitting curve.

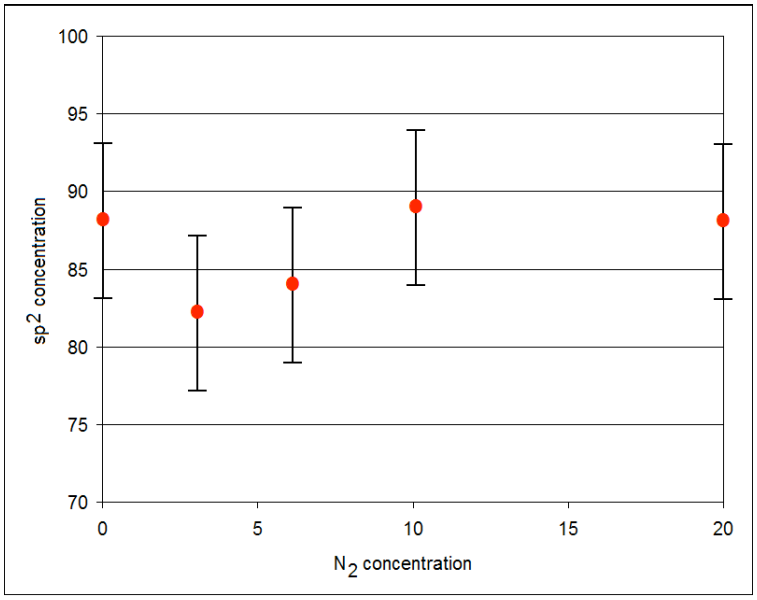

Fig. 3.17. Concentration of sp^2 bonding experimentally determined for a-C films deposited on silicon wafer substrates.

The general trend of growing sp^2 bonding concentration in silicon substrate a-C films with increasing N_2 deposition atmosphere is no different than that seen in the PTFE substrate films. However, simultaneous deposition onto silicon and PTFE substrates yields distinguishable a-C films. Structure of the a-C film does depend on the substrate onto which it is deposited. Bonding concentrations have the same general trend between the two substrates, but the absolute values do differ. It appears that the substrate influences the structure of the 220 nm thick films at around 12 Å from the film's surface. The silicon substrate more tightly constrains the sp^2 bonding concentrations of the films; the range of sp^2 concentrations of silicon wafer substrate films is 7%, where in PTFE substrate films the range is 19%.

3.3.3 Kα XES of a-C Films on Silicon Substrates

Carbon Kα (2p → 1s) XES spectra of a-C films deposited on silicon substrates (Fig. 3.18) show that there is essentially no difference in XES between the films deposited in 3 to 20% N_2 atmosphere. The XES spectra discussed in Section 3.2.3 are essentially identical to the spectra here, thus it can be further concluded that depositing a-C films on PTFE or silicon under similar conditions does not have an effect on the 2p occupied carbon states.

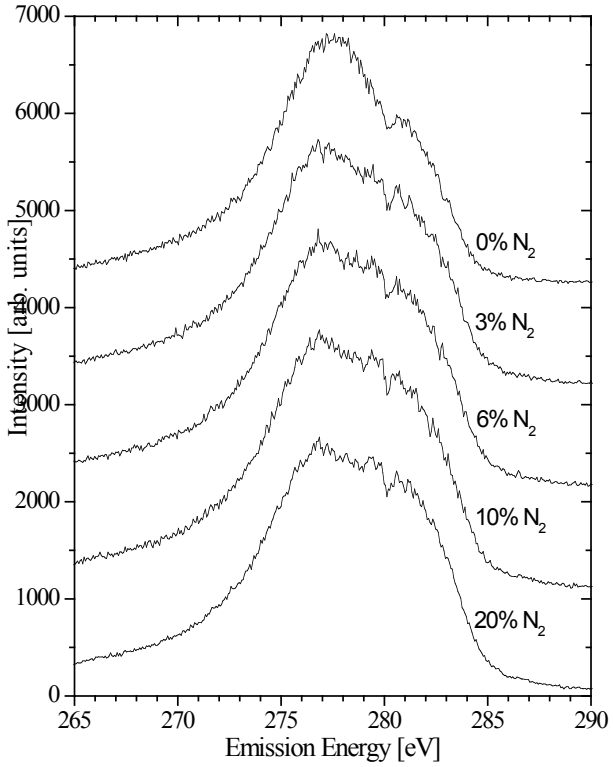

Fig. 3.18. Kα XES spectra of a-C films deposited on silicon substrates in varying N_2 atmospheres.

3.3.4 Nitrogen Absorption of Silicon Substrate a-C Films

Absorption measurements of the a-C films deposited on silicon substrates were taken at the N 1s → 2p (CB) edge (Fig. 3.19). The N 1s absorption spectrum of the film deposited in 0% N_2 atmosphere was disregarded since the film contains no nitrogen atoms and TEY measurements produced a constant absorption spectrum overlapped with noise, as expected. Spectral differences cannot be seen in the films deposited in N_2 atmospheres of 6 to 20%. A measurable difference between the 3% and 6 to 20% films is the ratio of the intensity of the two low energy π* features. That ratio changes from the 3% film to the 6% film, and then remains closely the same above and including the 6% film. There is also a small shoulder in the 3% film at 403.5 eV, which is absent in the other films. It is thus concluded that the nitrogen atoms interact with carbon and have the same bonding configuration in the

films deposited in 6% and higher N_2 atmospheres. Also, nitrogen atoms do not appear to interact with each other in the a-C films, since spectral differences would arise between all N 1s → 2p (CB) absorption spectra of different nitrogen concentrations.

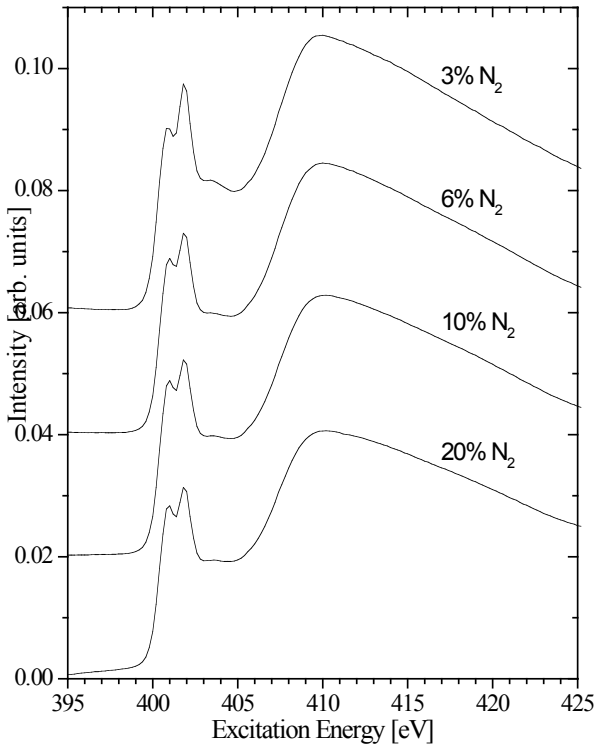

Fig. 3.19. N 1s absorption spectra of a-C films deposited on silicon substrates in various N_2 concentration atmospheres.

3.4 Nanodiamond

3.4.1 Varying Bias Voltage Deposition

C 1s absorption measurements of nanodiamond films deposited in a 1% CH_4 atmosphere while varying bias voltage were taken (Fig. 3.20). All the sp^2 concentrations of these films are between 2 $^{+5\%}_{-2\%}$ and 6% ± 5%. The spectra exhibit

the characteristic excitonic feature of diamond at 289.5 eV. Varying the bias voltage at the time of deposition in 1% CH_4 atmosphere appears to have little effect on the nanodiamond structure.

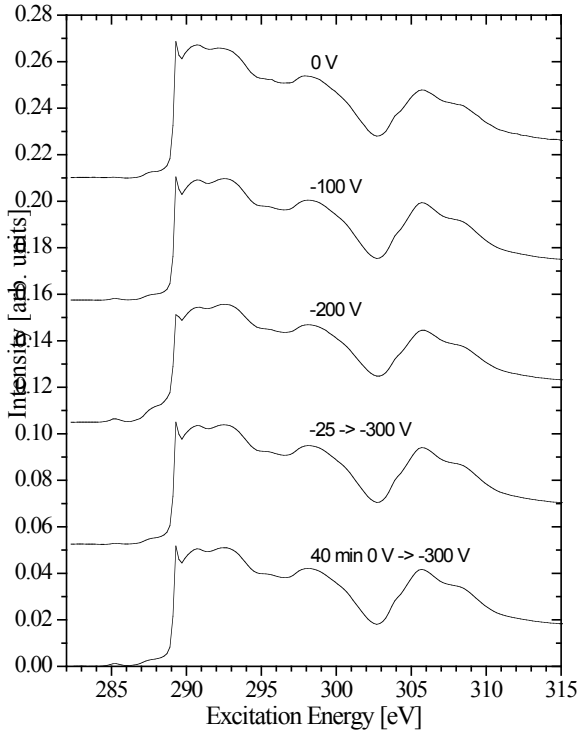

Fig. 3.20. C 1s absorption of nanodiamond samples deposited in a 1% CH_4 atmosphere with varying bias voltage. All sp^2 concentrations are calculated to be between 2 $^{+5\%}_{-2\%}$ and 6% ± 5%.

3.4.2 0 Bias Voltage Deposition

When bias voltage was held constant at 0 V, CH_4 atmosphere was increased from 1 to 100%. Absorption measurements (Fig. 3.21) show how the intensities of the C 1s → π* resonances change with CH_4 atmosphere. The absorption intensity at 285.5 eV increases with rising CH_4 atmosphere, but then falls down below maximum as methane is increased to 100%. The excitonic feature is diminished with additional CH_4 atmosphere. Calculated sp^2 concentrations change as shown in Fig. 3.22, with a steady increase up to 50% CH_4 atmosphere, followed by a decline

to 100% CH_4. The maximum sp^2 concentration achieved with a 0 V bias is 25% ± 5% at 50% CH_4, with a minimum of 3% $^{+5\%}_{-3\%}$ at 1% CH_4.

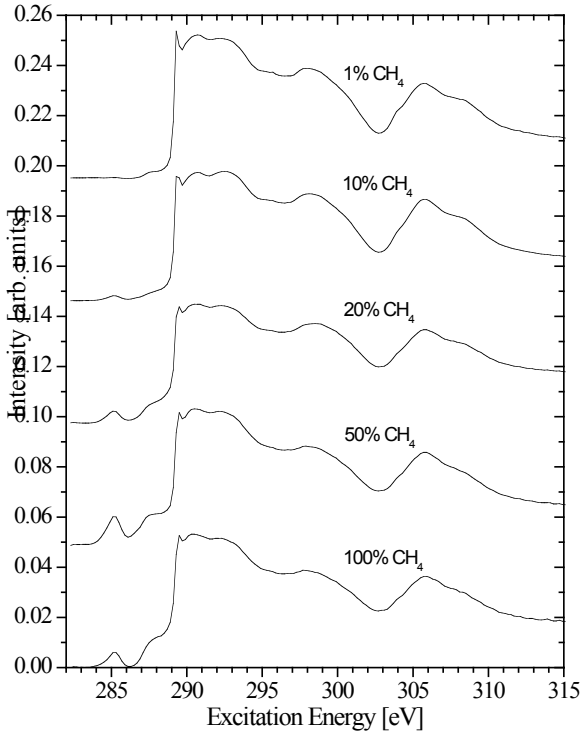

Fig. 3.21. C 1s absorption of nanodiamond samples deposited in varying CH_4 atmospheres with 0 V bias.

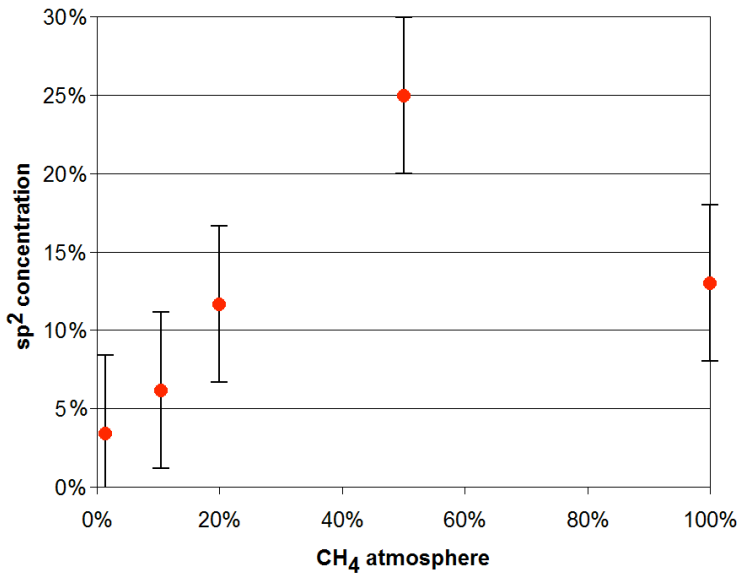

Fig. 3.22. Concentration of sp^2 bonding experimentally determined for nanodiamond samples deposited in varying CH_4 atmospheres with 0 V bias.

3.4.3 –300 V Bias Deposition

Bias voltage was then held constant at –300 V, while the CH_4 atmospheric concentration was increased from 2 to 50%. Absorption measurements (Fig. 3.23) show a similar trend to the ones in Fig. 3.21, with an increase in intensity at 285.5 eV, followed by a decrease. Calculated sp^2 concentrations change as shown in Fig. 3.24. A maximum of 13% ± 5% sp^2 concentration is achieved with a 20% CH_4 atmosphere, and minima of 6% ± 5% sp^2 are at 2% and 50% CH_4.

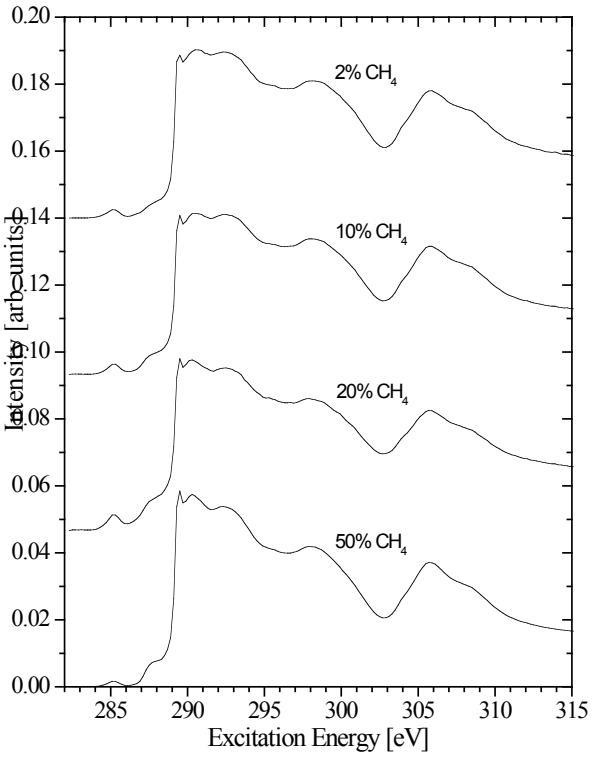

Fig. 3.23. C 1s absorption of nanodiamond samples deposited in varying CH_4 atmospheres with a –300 V bias.

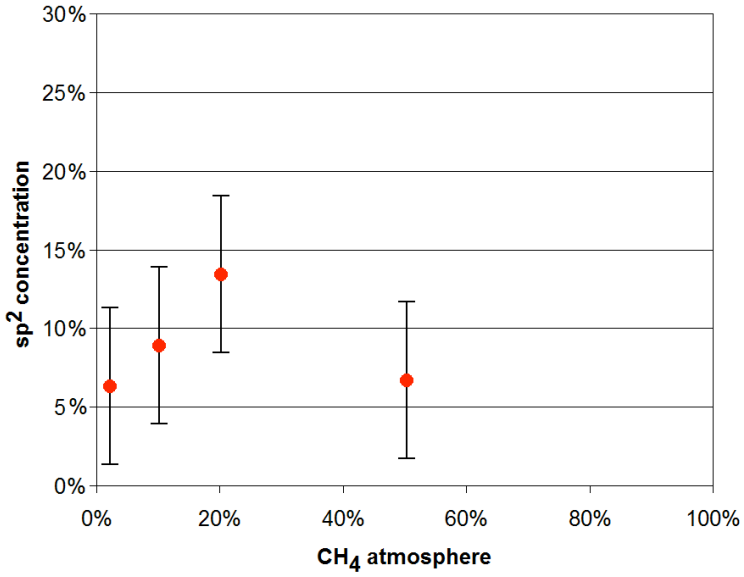

Fig. 3.24. Concentration of sp^2 bonding experimentally determined for nanodiamond samples deposited in varying CH_4 atmospheres with –300 V bias.

SUMMARY

A method is presented to analyze the structure of π* bands in the NEXAFS spectra of a-C and nanodiamond films to determine their sp^2 bonding concentration, which will serve to associate their electronic structure with their physical properties, such as hardness, thermal conductivity, chemical stability and wear resistance. This method can be further expanded to include all carbon nanostructures and other carbon systems, provided a detailed picture of its electronic structure is available. This method also addresses and overcomes many of the problems in previous methods in determining the sp^2 concentration of a carbon sample. Improvements over previous methods include modeling the ionization potential with an exponentially decaying post-edge step, extending the absorption measurement to 340 eV for proper ionization potential fitting, and correctly identifying the π* features in a-C spectra.

The principal chemical changes occurring when a-C films were deposited in increasing nitrogen atmosphere concentrations onto PTFE and silicon substrates consisted of an increase of sp^2 bonded atoms. The sp^2 concentrations of films deposited on PTFE substrates increased from 74 to 93% ± 5% as the nitrogen atmosphere during deposition increased from 0 to 20%. Films deposited on silicon substrates followed the same general trend. In both sets of films, the sp^2 bonding concentration reaches a maximum level when deposited in 10% nitrogen atmosphere, where no further increase in sp^2 bonding can be achieved with increased N_2 atmosphere. However, the finer near-surface structure of the film is influenced by the substrate onto which it is deposited; the silicon substrate more tightly constrains the range of sp^2 bonding concentrations of the films. Emission measurements show that there is little dependence on the substrate of the valence

band structure of the carbon films. However, nitrogen doping of the carbon film changes the occupied 2p carbon states. The 2p states remain the same for non-zero amounts of doping.

Nanodiamond films deposited onto treated silicon wafer substrates by hot filament chemical vapour deposition, with their exceptional hardness, introduce great potential applications. Spectroscopically, diamond and nanodiamond films are nearly the same. The basic difference arises in the low energy π^* feature, where higher spectral height implies greater sp^2 bonding in the film. Varying bias voltage during deposition of nanodiamond films in 1% CH_4 atmosphere has little effect on their sp^2 concentrations, which remained between $2\,^{+5\%}_{-2\%}$ and $6\% \pm 5\%$. The atmospheric concentration of CH_4 does, however, have an effect on sp^2 concentration. With bias voltage held constant at 0 V, sp^2 concentrations increased from $3\% \pm 5\%$ to a maximum of $25\% \pm 5\%$ sp^2 in 1 – 50% CH_4, followed by a drop to $13\% \pm 5\%$ at 100% CH_4. Bias voltage was then changed to –300 V and held constant for a series of depositions. Calculated sp^2 concentrations ranged from 6 – $13\% \pm 5\%$, with the maximum at 20% CH_4 atmosphere and minima at 1% and 50% CH_4.

We conclude that fitting and analyzing XAS spectra allows accurate and routine determinations of the sp^2 bonding concentrations in amorphous carbon and nanodiamond films.

APPENDIX

A Fitting Functions

A.1 Ionization Potential Fitting Function

In absorption spectra, the ionization potential (IP) appears as a step-like increase in absorption intensity followed by decay. It is best modeled by convolving a step function with a Gaussian, and, slightly above the step, applying an exponential decay. Here it is assumed that the intrinsic lineshape of the continuum step is quite narrow compared to the instrumental broadening. The natural width of the 1s core hole in carbon is 0.09 eV [116, 117], which is less than the instrumental resolution during XAS measurements. Broadening the step function with a Gaussian (instrumental broadening) is preferred over a Lorentzian (lifetime broadening) in this case. If instrumental resolution were much greater than the lifetime broadening, a Lorentzian would instead be convoluted with the step function. However, the formula used is

$$I_{step} = H\left[\frac{1}{2} + \frac{1}{2}erf\left(\frac{E-P}{\Gamma_G/1.665}\right)\right], \qquad \mathrm{E} \le \mathrm{P} + \Gamma_G, \qquad \text{(A.1a)}$$

$$I_{step} = H\left[\frac{1}{2} + \frac{1}{2}erf\left(\frac{E-P}{\Gamma_G/1.665}\right)\right]e^{-d(E-P-\Gamma)}, \qquad \mathrm{E} > \mathrm{P} + \Gamma_G, \qquad \text{(A.1b)}$$

where P is the position of the inflection point of the step, H is the height of the function immediately above the step, Γ_G is the width step (FWHM of the step, 1 eV is used), d is the exponential decay coefficient, and E is energy [27]. The decay

(d = 0.00676/eV), which matches that of the absorption cross section of solid carbon [19], is applied above the step to avoid distorting the shape of the step region. The height, H, is chosen to match the absorption intensity of the carbon spectrum between 320 – 340 eV, but not exceed it at any point. The inflection point, or IP onset, is set at approximately 289 eV for the samples measured.

A.2 Gaussian Fitting Function

The Gaussian fitting function is given by the formula

$$I(E) = \frac{A}{w}\sqrt{\frac{4\ln(2)}{\pi}}e^{\frac{-4\ln(2)(E-E_c)^2}{w^2}}, \qquad \text{(A.2)}$$

where A is the peak area, w is the FWHM of the peak and E_c is the center position.

B Principal Errors in Fitting Procedure

B.1 Statistical Error

B.1.1 Variations Due to Fitting Method

Spectral fits are done according to the method outlined in this paper, but it is expected that an exact reproduction of a fit cannot be made every time. Nearly perfect overlap of the fitted function and the spectrum can be obtained even with small variations of the Gaussian functions from one fit to the next. Since it is essentially the integrated area of the Gaussians deemed π* that contribute to the sp^2 concentration of the film, the resulting sp^2 concentration varies slightly from one fit to the next. Repeated fits of the same spectrum yield sp^2 concentrations with a 3% standard deviation.

B.1.2 Reproducibility of Spectra

As discussed in Appendix B.2.3, spectra of C_{60} are remarkably similar when measured at three different beamlines at the ALS, even more so when measured at the same beamline. Differences may arise from instrumental broadening, which, to varying degrees, will widen features in the spectrum. Intensities or widths of the features in these different spectra do vary by small amounts, but the ratios of π*/total integrated intensity do not change much. Since the a-C films in this study have only been measured at beamline 8.0.1 of the ALS, it can be assumed that reproducibility will be as great as with C_{60}.

Sufficient data to quantify the error involved with spectral reproducibility are not available. It would be necessary to measure the same sample with the same experimental settings and beamline many times to be able to gauge the true magnitude of this effect.

B.2 Systematic Error

B.2.1 Varying Integration Area

For the method outlined in this paper, the total area integration is done from 280 – 320 eV (40 eV window). Berger *et al.* [104] increased the total area integration window from 20 – 110 eV on their samples and found that the calculated fraction of sp^2 bonded carbon atoms increased by 4%. In this study the energy window was similarly increased for a sample, and it was also found that the sp^2 fraction varied by only a few percent. Since a 40 eV integration area window has been determined to exclude problems associated with a small (20 eV) area and a large (>50 eV) area, the associated error is negligible.

B.2.2 Gold Mesh

As discussed in Section 1.3.1, a transparent gold mesh is situated in front of the sample chamber to detect the flux of photons incident on the sample. It serves to negate the effects of changes in photon flux due to the storage ring and absorption of photons in the monochromator or other optics in the beamline. Due to carbon contamination, the mesh will absorb at the carbon 1s → 2p edge. When measuring at that same edge, the absorption spectrum of the sample will be artificially high. At beamline 8.0.1 of the ALS, the gold mesh is frequently cleaned so that carbon contamination is at a minimum. But, including a measurement of C_{60} in the sample set can minimize this already small error. The effect of carbon absorption in the gold mesh appears in the numerator and denominator of Eqn. 3.2 and is essentially cancelled out. A systematic error in the incident flux is equally applied to both the carbon sample and reference (C_{60}) sample, normalizing itself out.

B.2.3 Calibration Sample

Any errors in fitting the calibration sample, C_{60}, will affect the calculated sp^2 values of the carbon sample in question. Since the effect of all C_{60} fitting errors are applied in the same way to all of the samples in a set, the calculated sp^2 values will be affected by the same amount. For example, if the true, or error free, value of the π^*/total intensity ratio of C_{60} is 0.09, but 0.10 was determined, then all sp^2 values for a-C films will be $1/10^{th}$ lower than their true value (excluding each of their own statistical errors). This error will, of course, shift all calculated sp^2 values in the same direction by the same proportion. It will not affect the trend of a data set.

To minimize this systematic error, a set of samples must be measured at the same time as the reference sample, C_{60}. For example, if all the carbon absorption spectra taken during the same run are enhanced in the π^* region, the effect will be cancelled out in the sp^2 calculation by the same enhancement of the C_{60} spectrum (double normalization). It is easy to see that if the same C_{60} spectrum is used to calculate the sp^2 concentration of films from one run of measurements to another, this error will not be minimized. However, calculating the π^*/total intensity ratios of several C_{60} spectra from three different beamlines at the ALS yield values that are very close to each other (0.12), which indicates that this error, even when not taken into account, is minimal.

The same statistical error discussed in Appendix B.1.1 applies to fitting C_{60} as well.

B.3 Total Error Derivation

Table B.1 shows the determined and estimated maximum errors involved in determining the sp^2 concentrations of carbon films. Total errors are determined by their quadrature sum of errors

$$\sigma_{total} = \sqrt{\left(\Sigma \sigma_i^2\right)}, \qquad \text{(B.1)}$$

where σ_{total} is the total error derived from the contribution of the individual errors, σ_i.

Table B.1. Determined and estimated maximum errors in determining the sp^2 concentrations of carbon films. Individual error contributions are combined in quadrature.

Statistical Error		Determined	Maximum
B.1.1	variations of fitting method	3%	3%
B.1.2	spectral reproducibility	N/A	3%
B.2.3	calibration sample	3%	3%
Systematic Error			
B.2.1	integration area	~0	4%
B.2.2	gold mesh	~0	~0
B.2.3	calibration sample	~0	4%
Total		**4.2%**	**7.7%**

The determined total error of 4.2% (5% is used to be conservative) is based mostly on the variations of the fitting method, which affect both the carbon film sample and the reference sample, C_{60}. Systematic errors are minimized, and estimated to be approximately zero. The maximum individual errors are reasonable estimates of their maximum error contribution. Assuming systematic errors are not minimized, total error in the determination of sp^2 concentration is 7.7%, which can be reduced to 5.7% statistical and 5.2% systematic errors. Each of those systematic errors will affect the resulting sp^2 concentrations in the same direction, such that the trends in those data are unaffected.

C Radiation Damage

Studying radiation damage of samples is a research field in itself, but is worth mentioning here without going into great detail. Radiation damage from soft x-rays [118, 119] has not been studied in as much detail as from hard x-rays, high energy electrons and gamma radiation. Radiation damage of polymers can take several forms, such as loss of crystallinity, loss of mass, or chemical modification [120, 121]. The intense synchrotron radiation appears to have caused damage to these a-C films (Fig. C.1 and Fig. C.2). During emission (XES) measurements, the sample is exposed to high flux radiation to achieve high count rates. After only minutes the exposed area attains visible damage. The nature of this damage has not been investigated. For absorption measurements the flux is lowered significantly and the sample is shifted to the right so that the exposed area is now to the left of the damaged portion (Fig. C.1 and Fig. C.2). There is no visible damage to this section of the film. Chemical differences between damaged and undamaged regions have not been investigated, but it is preferred that all absorption spectra are measured on regions that are undamaged before and after measurement.

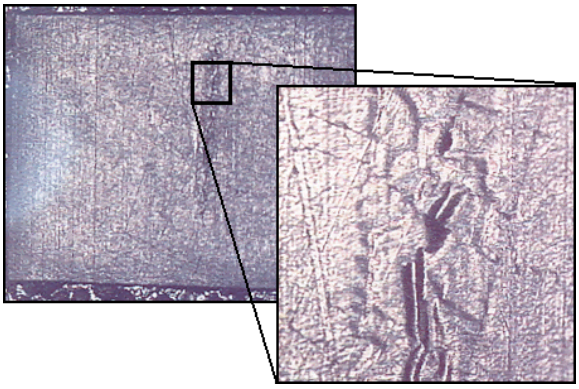

Fig. C.1. Light microscopy picture of a-C deposited on a PTFE substrate in 3% N_2 atmosphere after exposure to synchrotron radiation (2.5x and 20x magnification). Emission measurements lead to the darkened vertical line; absorption measurements were made to the far left of that and the sample remained visibly undamaged.

Fig. C.2. Light microscopy picture of a-C film deposited on silicon substrate in 20% N_2 atmosphere after exposure to synchrotron radiation (2.5x magnification). Emission measurements lead to the discoloured (darkened) vertical section; absorption measurements were made to the far left of that. Handling the sample after measurements caused the two horizontal scratch lines.

D Fitted π* Peak Parameters

Table D.2 includes the necessary Gaussian parameters to replicate fits of the π* regions in a-C films deposited on PTFE and silicon substrates.

Table D.2. Fitted π* peak parameters for a-C films deposited on PTFE and silicon substrates. All values have an uncertainty of ±1 in their last decimal place.

Nitrogen	π* Peaks of **PTFE** Substrate Films			π* Peaks of **Si** Substrate Films		
Atmosphere	π* Position	Height	FWHM	π* Position	Height	FWHM
0%	285.41	0.0175	1.993	285.42	0.0220	1.931
	287.34	0.0170	2.038	287.13	0.0194	1.834
	288.57	0.0107	1.328	288.48	0.0152	1.399
3%	285.90	0.0174	1.943	286.64	0.022	3.026
	286.88	0.0118	0.966	286.85	0.007	0.634
	288.08	0.0235	1.874	288.25	0.014	1.641
6%	285.92	0.0148	1.817	286.66	0.0166	3.083
	286.85	0.0104	0.840	286.83	0.0115	0.817
	288.03	0.0285	2.034	288.18	0.0199	1.675
10%	285.98	0.0159	1.908	286.18	0.0171	1.996
	286.83	0.0108	0.828	286.86	0.0106	0.679
	288.16	0.0313	2.047	288.04	0.0291	2.015
20%	285.91	0.0160	1.877	286.09	0.0169	1.911
	286.82	0.0094	0.671	286.86	0.0121	0.763
	287.97	0.0301	2.293	288.05	0.0290	1.976

REFERENCES

[1] J. Díaz, S. Anders, X. Zhou, E.J. Moler, S.A. Kellar, Z. Hussain, Phys. Rev. B **64**, 125204 (2001).

[2] J. Robertson, Surf. Coat. Technol. **50**, 185 (1992).

[3] A. Grill, *Cold Plasmas in Materials Fabrication* (IEEE Press, New York, 1994).

[4] M.S. Sheu, D.M. Hudson, I.K. Loh, *Encyclopedic Handbook of Biomaterials and Bioengineering* Vol. 1 ed. by D.L. Wise, D.J. Trantolo, D.E. Altobelly, M.J. Yaszemeki, J.D. Gresser, E.R. Schwartz, M. Dekker (New York, 1995).

[5] B.S. Satyanarayana, A. Hart, W.I. Milne, J. Robertson, Appl. Phys. Lett. **71**, 1430 (1997).

[6] W.C. Chan, M.K. Fung, I. Bello, C.S. Lee, S.T. Lee, Diamond Relat. Mater. **8**, 1732 (1999).

[7] V.N. Vasilets, A. Hirose, Q. Yang, A. Singh, R. Sammynaiken, M. Foursa, Y.M. Shulga, Appl. Phys. A **79**, 2079 (2004).

[8] H.S. Shim, N.K. Agarwal, A.D. Haubold, J. Bioeng. **1**, 45 (1976).

[9] *Physics Web – Undulators*. Available from <http://physicsweb.org/articles/world/11/1/3/1/world-11-1-3-2>.

[10] J.J. Jia, T.A. Callcott, J. Yurkas, A.W. Ellis, F.J. Himpsel, M.G Samant, J. Stöhr, D.L. Ederer, J.A. Carlisle, E.A. Hudson, L.J. Terminello, D.K. Skuh, R.C.C. Perera, Rev. Sci. Instrum. **66**, 1394 (1995).

[11] J. Nordgren, J.-H. Guo, J. Electron Spectrosc. Relat. Phenom. **110-111**, 1 (2000).

[12] *High Resolution and Flux for Materials and Surface Science – Beamline 8.0.1*. Available at <http://www-als.lbl.gov/als/als_users_bl/8.0.1-Overview.pdf>.

[13] M.O. Krause, J.H. Oliver, J. Phys. Chem. Ref. Data **8**, 329 (1979).

[14] *X-Ray Data Booklet*, edited by A. C. Thompson and D. Vaughan (Lawrence Berkeley National Laboratory, Berkeley, 2001).

[15] M.P. Seah, W.A. Dench, Surf. Interf. Anal. **1**, 2 (1979).

[16] G. Ertl, J. Küppers, *Low Energy Electrons and Surface Chemistry* (VCH, 1985), 2nd ed.

[17] D. Atwood, *Soft X-Rays and Extreme Ultraviolet Radiation: Principles and Applications* (Cambridge University Press, New York, 1999).

[18] *X-Ray Data Booklet*, edited by A.C. Thompson and D. Vaughan (Lawrence Berkley National Laboratory, Berkeley, 2001). Available from <http://xdb.lbl.gov/Section3/Sec_3-2.html>.

[19] B.L. Henke, E.M. Gullikson, J.C. Davis, At. Data Nucl. Data Tables **54**, 181 (1993).

[20] A. Moewes, *Soft X-Ray Fluorescence Spectroscopy* (CAMD Summer School, Louisiana State University, Baton Rouge, LA, USA, June 2000).

[21] M.O. Krause, J. Phys. and Chem. Ref. Data **8**, 307-327 (1979).

[22] E.L. Shirley, J. El. Spec. **110-111**, 305 (2000).

[23] K. Feser, Phys. Rev. Lett. **28**, 1013 (1972).

[24] W. Hink, H. Paschke, Phys. Rev. A **4**, 507 (1971).

[25] H.L. Hagedoorn, A.H. Wapstra, Nucl. Phys. **15**, 146 (1960).

[26] W. Hanke, J. Wernisch, C. Pohn, X-ray Spectrometry **14**, 43 (1985).

[27] J. Stöhr, *NEXAFS Spectroscopy* (Springer, New York, 1996), Vol. 25.

[28] J. Frenkel, Phys. Rev. **37**, 1276 (1931).

[29] G.G. Macfarlane, T.P. McLean, J.E. Quarrington, V. Roberts, Phys. Rev. **108**, 1377 (1957).

[30] R.J. Elloitt, Phys. Rev. **108**, 1384 (1957).

[31] C. Kittel, *Introduction to Solid State Physics* (John Wiley & Sons, Inc., New York, 1996), 7th ed.

[32] G.K. Wannier, Phys. Rev. **52**, 191 (1937).

[33] N.F. Mott, Trans. Faraday Society **34,** 822 (1938).

[34] S.O. Kasap, *Principles of Electronic Materials and Devices* (McGraw-Hill, New York, 2002), 2nd ed.

[35] *Hybridization, Flash Animations.* Available from <http://www.mhhe.com/physsci/chemistry/essentialchemistry/flash/hybrv18.swf>.

[36] *The Creative Science Center – The Discovery of C_{60}.* Available from <http://www.creative-science.org.uk/c60info.html>.

[37] S. Satpathy, V.P. Antropov, O.K. Andersen, O. Jepsen, O. Gunnarsson, A.I. Liechtenstein, Phys. Rev. B **46**, 1773 (1992).

[38] L.J. Terminello, D.K. Shuh, F.J. Himpsel, D.A. Lapiano-Smith, J. Stöhr, D.S. Bethune, G. Meijer, Chem. Phys. Lett. **182,** 491 (1991).

[39] R.C. Haddon, L.E. Brus, K. Raghavachari, Chem. Phys. Lett. **125,** 459 (1986).

[40] P.W. Fowler, and J. Woolrich, Chem. Phys. Lett. **127,** 78 (1986).

[41] J.-H. Guo, P. Glans, P. Skytt, N. Wassdahl, J. Nordgren, Phys. Rev. B **52**, 10681 (1995).

[42] J.-H. Guo, S.M. Butorin, N. Wassdahl, T. Warwick, J. Nordgren, J. El. Spec. **114-116**, 885 (2001).

[43] J.-H. Guo, J. Nordgren, J. El. Spec. **110-111**, 105 (2000).

[44] E. Sohmen and J. Fink, Phys. Rev. B **47**, 14532 (1993).

[45] C.T. Chen, L.H. Tjeng, P. Rudolf, G. Meigs, J.E. Rowe, J. Chen, J.P. McCauley Jr, A.B. Smith III, A.R. McGhie, W.J. Romanow, E.W. Plummer, Nature **352**, 603 (1991).

[46] Y. Luo, H. Agren, F. Gel'mukhanov, J.-H. Guo, P. Skytt, N. Wassdahl, J. Nordgren, Phys. Rev. B **52**, 14479 (1995).

[47] J.-H. Guo, D.E. Ellis, D.J. Lam, Chem. Phys. Lett. **184,** 418 (1991).

[48] B. Wastberg, S. Lunell, C. Enkvist, P.A. Bruhwiler, A.J. Maxwell, N. Martensson, Phys. Rev. B **50**, 13031 (1994).

[49] E.Z. Kurmaev, A. Moewes, T. Ida, S. Danielache, K. Endo, I.O. Bashkin, A.I. Harkunov, A.P. Moravsky, J. Mol. Struct. (Theochem) **639**, 27 (2003).

[50] S. Saito, A. Oshiyama, Phys. Rev. Lett. **66**, 2637 (1991).

[51] H. Romberg, M. Roth, J. Fink, Phys. Rev. B **49**, 1427 (1994).

[52] E. Sohmen, J. Fink, W. Kratschmer, Europhys. Lett. **17**, 51 (1992).

[53] T. Kaambre, L. Qian, J.E. Rubensson, J.-H. Guo, C. Sathe, J. Nordgren, J.P. Palmqvist, U. Jansson, Eur. Phys. J. D **16**, 357-360 (2001).

[54] R.A. Assink, J.E. Schirber, D.A. Loy, B. Morosin, G.A. Carlson, J. Mater. Res. **7**, 2136 (1992).

[55] G.A. Samara, L.V. Hansen, R.A. Assink, B. Morosin, J.E. Schirber, D.A. Loy, Phys. Rev. B **47**, 4756 (1993).

[56] R. Taylor, J.P. Parsons, A.G. Avent, S.P. Rannard, T.J. Dennis, J.P. Hare, H.W. Kroto, D.R.M. Walton, Nature **351**, 277 (1991).

[57] *MikroMasch SPM – Highly Ordered Pyrolytic Graphite*. Available from <http://www.spmtips.com/products/hopg/>.

[58] R. Chang, *Chemistry* (McGraw-Hill, New York, 1998), 6th ed.

[59] R.A. Rosenberg, P.J. Love, V. Rehn, Phys. Rev. B 33, 4034 (1986).

[60] F.L. Coffman, R. Cao, P.A. Pianetta, S. Kapoor, M. Kelly, L.J. Terminello, Appl. Phys. Lett. **69**, 568 (1996).

[61] P.E. Batson, Phys. Rev. B **48**, 2608 (1993).

[62] E.J. Mele, J.J. Ritsko, Phys. Rev. Lett. **43**, 68 (1979).

[63] J.A. Carlisle, S.R. Blankenship, R.N. Smith, E.L. Shirley, L.J. Terminello, J.J. Jia, T.A. Callcott D.L. Ederer, J. El. Spec. **103**, 839 (1999).

[64] J.A. Carlisle, S.R. Blankenship, L.J. Terminello, J.J. Jia, T.A. Callcott, D.L. Ederer, R.C.C. Perera, F.J. Himpsel, J. El. Spec. **110**, 323 (2000).

[65] P. Skytt, P. Glans, D.C. Mancini, J.-H. Guo, N. Wassdahl, J. Nordgren, Y. Ma, Phys. Rev. B **50**, 10457 (1994).

[66] Y. Ma, P. Skytt, N. Wassdahl, P. Glans, D.C. Mancini, J.-H. Guo, J. Nordgren, Phys. Rev. Lett. **71**, 3725 (1993).

[67] G. Comelli, J. Stöhr, C.J. Robinson, W. Jark, Phys. Rev. B **38**, 7511 (1988).

[68] A.J. Papworth, C.J. Kiely, A.P. Burden, S.R.P. Silva, G.A.J. Amaratunga, Phys. Rev. B **62**, 12628 (2000).

[69] R. Gago, I. Jimenez, J.M. Albella, A. Climent-Font, D. Caceres, I. Vergara, J.C. Banks, B.L. Doyle, L.J. Terminello, J. Appl. Phys. **87**, 8174 (2000).

[70] *Materials Science – The Structure of Solids, Diamond*. Available from <http://chemed.chem.purdue.edu/genchem/topicreview/bp/materials/material1.html>.

[71] K.A. Jackson, M.R. Pederson, Phys. Rev. Lett. **67**, 2521 (1991).

[72] J. Nithianandam, Phys. Rev. Lett. **69**, 3108 (1992).

[73] Y. Ma, N. Wassdahl, P. Skytt, J.-H. Guo, J. Nordgren, P.D. Johnson, J-E. Rubensson, T. Boske, W. Eberhardt, S.D. Kevan, Phys. Rev. Lett. **69**, 2598 (1992).

[74] D.M. Gruen, A.R. Krauss, C.D. Zuiker, R. Csencsits, L.J. Terminello, J.A. Carlisle, I. Jimenez, D.G.J. Sutherland, D.K. Shuh, W. Tong, F.J. Himpsel, Appl. Phys. Lett. **68**, 1640 (1996).

[75] C. Lenardi, P. Piseri, V. Briois, C.E. Bottani, A. Li Bassi, P. Milani, J. Appl. Phys. **85**, 7159 (1999).

[76] J. Díaz, S. Anders, X. Zhou, E.J. Moler, S.A. Kellar Z. Hussain, J. El. Spec. **103,** 545 (1999).

[77] J.F. Morar, F.J. Himpsel, G. Hollinger, G. Hughes, J. L. Jordan, Phys. Rev. Lett. **54**, 1960 (1985).

[78] P.E. Batson, Phys. Rev. Lett. **70**, 1822 (1993).

[79] M. Lubbe, P.R. Bressler, D. Drews, W. Braun, D.R.T. Zahn, Diamond Relat. Mater. **7**, 247-249 (1998).

[80] W.F. Pong, Y.K. Chang, H.H. Hsieh, M.H. Tsai, K.H. Lee, T.E. Dann, F.Z. Chien, P.K. Tseng, K.L. Tsang, W.K. Su, L.C. Chen, S.L. Wei, K.H. Chen, D.M. Bhusari, Y.F. Chen, J. El. Spec. **92**, 115 (1998).

[81] Y.K. Chang, H.H. Hsieh, W.F. Pong, M.H. Tsai, F. Z. Chien, P.K. Tseng, L.C. Chen, T.Y. Wang, K.H. Chen, D.M. Bhusari, J.R. Yang, S.T. Lin, Phys. Rev. Lett. **82**, 5377 (1999).

[82] W.F. Pong, C.L. Yueh, Y.D. Chang, M.-H. Tsai, Y.K. Chang, Y.Y. Chen, J.F. Lee, S.L. Wei, C.Y. Wen, L.C. Chen, K.H. Chen, I.N. Lin, H.F. Cheng, J Synchrotron Rad. **8**, 145-149 (2001).

[83] Y.H. Tang, X.T. Zhou, Y.F. Hu, C.S. Lee, S.T. Lee, T.K. Sham, Chem. Phys. Lett. **372**, 320 (2003).

[84] L.J. Huang, I. Bello, W.M. Lau, S.T. Lee, P.A. Stevens, B.D. DeVries, J. Appl. Phys. **76**, 7483 (1994).

[85] Q. Yang, C. Xiao, W. Chen, A. Hirose, Diamond Relat. Mater. **13**, 433 (2004).

[86] G. Galli, R.M. Martin, R. Car, M. Parrinello, Phys. Rev. Lett. **62**, 555 (1989).

[87] C.Z. Wang, K.M. Ho, Phys. Rev. Lett. **71**, 1184 (1993).

[88] C. H. Lee, W.R.L. Lambrecht, B. Segall, P.C. Kelires, T. Frauenheim, U. Stephan, Phys. Rev. B **49**, 11448 (1994).

[89] N.A. Marks, D.R. McKenzie, B.A. Pailthorpe, M. Bernasconi, M. Parrinello, Phys. Rev. Lett. **76**, 768 (1996).

[90] D.G. McCulloch, D.R. McKenzie, C.M. Goringe, Phys. Rev. B **61**, 2349 (2000).

[91] I. Jimenez, R. Gago, J.M. Albella, D. Caceres, I. Vergara, Phys. Rev. B **62**, 4261 (2000).

[92] S. Bhattacharyya, M. Lubbe, P.R. Bressler, D.R.T. Zahn, F. Richter, Diamond Relat. Mater. **11**, 8 (2002).

[93] E. Broitman, N. Hellgren, Zs. Czigany, R.D. Twesten, J. Luning, I. Petrov, L. Hultman, B.C. Holloway, J. Vac. Sci. Technol. A **21**, 851 (2003).

[94] E.H. Lee, D.M. Hembree, G.R. Rao, L.K. Mansur, Phys. Rev. B **48**, 15540 (1993).

[95] C.V. Cooper, C.P. Beetz, B.W. Buchholtz, P.J. Wilbur, R. Wei, Diamond Relat. Mater. **3**, 534 (1994).

[96] J.C. Lascovich, R. Giorgi, S. Scaglione, Appl. Surf. Sci. **47**, 17 (1991).

[97] S. Scaglione, R. Giorgi, J.C. Lascovich, G. Ottaviani, Surf. Coat. Technol. **47**, 287 (1991).

[98] A. Fuchs, J. Scherer, K. Jung, H. Ehrhardt, Thin Solid Films **232**, 51 (1993).

[99] S. Hüfner, *Photoelectron Spectroscopy* (Springer-Verlag, Berlin, 2003).

[100] J, Díaz, G. Paolicelli, S. Ferrar, F. Comin, Phys. Rev. B **54**, 8064 (1996).

[101] J.C. Lascovich, S. Scaglione, Appl. Surf. Sci. **78**, 17 (1994).

[102] G. Speranza, N. Laidani, Diamond and Relat. Mater. **13**, 445 (2004).

[103] G. Speranza, N. Laidani, Diamond and Relat. Mater. **13**, 451 (2004).

[104] D. Berger, D.R. McKenzie, P.J. Martin, Philos. Mag. Lett. **57**, 285 (1988).

[105] J.J. Cuomo, J.P. Doyle, J. Bruley, J.C. Liu, J. Vac. Sci. Technol. A **9**, 2210 (1991).

[106] P.J. Fallon, V.S. Veerasamy, C.A. Davis, J. Robertson, G.A. Amaratunga, W.I. Milne, J. Koskinen, Phys. Rev. B **48**, 4777 (1993).

[107] J. Bruley, D.B. Williams, J.J. Cuomo, P. Pappas, J. Microsc. **180**, 22 (1995).

[108] A.M. Mezzasalma, G. Mondio, F. Neri, S. Trusso, J. Appl. Phys. D **36**, 541 (2003).

[109] T.J. Titantah, D. Lamoen, Phys. Rev. B **70**, 075115 (2004).

[110] L.J. Terminello, D.K. Shuh, F.J. Himpsel, D.A. Lapiano-Smith, J. Stöhr, D.S. Bethune, G, Meijer, Chem. Phys. Lett. **182**, 491 (1991).

[111] V. Carravetta, H. Agren, L.G.M. Pettersson, O. Vahtras, J. Chem. Phys. **102**, 5589 (1995).

[112] L.G. Parratt, Phys. Rev. **56**, 295 (1939).

[113] R.L. Martin, D.A. Shirley, *Electron Spectroscopy, Theory, Techniques and Applications*, Vol. 1 ed. by C.R. Brundle, A.D. Baker, (Academic, New York, 1978).

[114] J. Hu, P. Yang, C.M. Lieber, Phys. Rev. B **57**, 3185 (1998).

[115] B. Kleinsorge, A.C. Ferrari, J. Robertson, W.I. Milne, S. Waidmann, S. Hearne, Diamond and Relat. Mater. **9**, 643 (2000).

[116] L.G. Parratt, , Rev. Mod. Phys. **31**, 616 (1959).

[117] F.C. Brown, Solid State Phys. **29**, 1 (1974).

[118] E.G. Rightor, A.P. Hitchcock, H. Ade, R.D. Leapman, S.G. Urquhart, A.P. Smith, G. Mitchell, D. Fisher, H.J. Shin, T. Warwick, J. Phys. Chem. B **101**, 1950 (1997).

[119] X. Zhang, C. Jacobsen, S. Lindaas, S. Williams, J. Vac. Sci. Technol. B **13**, 1477 (1995).

[120] D. Vesely, D. Finch, Electron Microsc. Anal. **7** (1985).

[121] T. Coffey, S.G. Urquhart, H. Ade, J. El. Spec. **122**, 65 (2002).